Nano Research

ISSN 1998-0124 CN 11-5974/O4
https://doi.org/10.26599/NR.2025.94908018

Research Article

Laser-stepwise-induced graphene with reduced sheet resistance enables electromagnetic shielding manipulation

Pengfei Chen[1,2], Yitong Xin[2,3], Haoran Zu[2,3], Xinrui Yang[1,2,4], Hao Feng[2,4], Wenxiang Xu[2], Yifan Chang[1,2], Zibo Chen[1,2], Wei Qian[2], Yong Lv[5], Huaqiang Fu[1,2](✉), Lin Ren[6], Daping He[1,2,4](✉)

[1] School of Materials Science and Engineering, Wuhan University of Technology, Wuhan 430070, China

[2] Hubei Engineering Research Center of Radio Frequency Microwave Technology and Application, School of Physics and Mechanics, Wuhan University of Technology, Wuhan 430070, China

[3] School of Information Engineering, Wuhan University of Technology, Wuhan 430070, China

[4] State Key Laboratory of Silicate Materials for Architectures, Wuhan University of Technology, Wuhan 430070, China

[5] Hubei Key Laboratory of Theory and Application of Advanced Material Mechanics, School of Physics and Mechanics, Wu Daping He han University of Technology, Wuhan 430070, China

[6] Hubei Longzhong Laboratory, Wuhan University of Technology Xiangyang Demonstration Zone, Xiangyang 441000, China

Nano Res., **Just Accepted Manuscript** • https://doi.org/10.26599/NR.2025.94908018

https://www.sciopen.com/journal/1998-0124 on Aug. 28, 2025

TABLE OF CONTENTS (TOC)

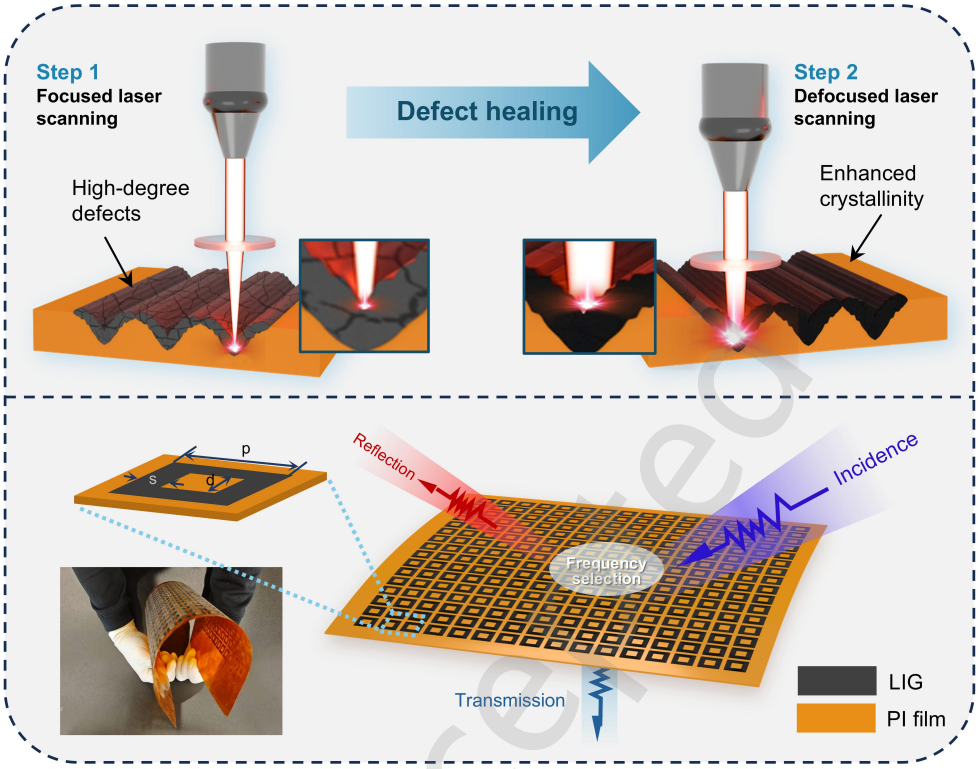

This work develops a laser-stepwise-induced graphene (LSIG) method that heals defects and promotes crystalline domain growth in laser-induced graphene (LIG). LSIG with reduced sheet resistance of 15 Ω sq^{-1} enables direct patterning of a flexible frequency-selective surface for electromagnetic wave manipulation, exhibiting an enhanced effective bandwidth of 4.92 GHz and a transmission coefficient of 0.057 at its resonant frequency.

Research Article

Laser-stepwise-induced graphene with reduced sheet resistance enables electromagnetic shielding manipulation

Pengfei Chen[1,2], Yitong Xin[2,3], Haoran Zu[2,3], Xinrui Yang[1,2,4], Hao Feng[2,4], Wenxiang Xu[2], Yifan Chang[1,2], Zibo Chen[1,2], Wei Qian[2], Yong Lv[5], Huaqiang Fu[1,2]✉, Lin Ren[6], and Daping He[1,2,4]✉

[1] School of Materials Science and Engineering, Wuhan University of Technology, Wuhan 430070, China
[2] Hubei Engineering Research Center of Radio Frequency Microwave Technology and Application, School of Physics and Mechanics, Wuhan University of Technology, Wuhan 430070, China
[3] School of Information Engineering, Wuhan University of Technology, Wuhan 430070, China
[4] State Key Laboratory of Silicate Materials for Architectures, Wuhan University of Technology, Wuhan 430070, China
[5] Hubei Key Laboratory of Theory and Application of Advanced Material Mechanics, School of Physics and Mechanics, Wu Daping He *han University of Technology, Wuhan 430070, China*
[6] Hubei Longzhong Laboratory, Wuhan University of Technology Xiangyang Demonstration Zone, Xiangyang 441000, China

Received: 31 July 2025; **Revised:** 28 August 2025; **Accepted:** 28 August 2025

*Address correspondence to Huaqiang Fu, fuhuaqiang@whut.edu.cn; Daping He, hedaping@whut.edu.cn

Cite this article: *Nano Research*, 2025, 18, 94908018.
https://doi.org/10.26599/NR.2025.94908018

ABSTRACT

Laser-induced graphene (LIG) technology enables the direct writing of functional films for flexible devices. However, the intrinsic amorphous structure, triggered by laser-induced ultrafast kinetics, leads to high sheet resistance. Herein, we report a designed laser-stepwise induced graphene (LSIG) method, which sequentially applies focused and defocused laser pulses to polyimide precursors to reduce sheet resistance. In this method, the focused laser pulse induces longitudinal heat penetration and diffusion through the substrate, enabling conversion of polyimide molecules into graphene, while the subsequent defocused pulse facilitates defect healing and crystalline domain growth, achieving a remarkably low sheet resistance of 15 Ω sq^{-1} for LSIG. The LSIG exhibits a decreased defect density and increased crystalline domain from Raman analysis. Compared with existing approaches involving chemical reduction or high-temperature treatment for LIG optimization, the LSIG methodology accomplishes single-step synthesis while maintaining experimental simplicity. Utilizing LSIG technology, we design and fabricate a flexible frequency-selective surface to demonstrate its potential in electromagnetic devices and systems.

Keywords: laser-stepwise-induced graphene, sheet resistance reduction, frequency-selective surface, electromagnetic shielding manipulation

INTRODUCTION

Graphene has emerged as a promising two-dimensional material because of its exceptional electrical, chemical, and mechanical properties [1-3]. Since 2004, graphene synthesis methodologies such as chemical vapor deposition [4, 5], liquid exfoliation [6, 7], and epitaxial growth [8, 9] have been extensively investigated. However, these methods present inherent scalability limitations due to their multi-step processing requirements and stringent environmental controls. In 2014, the development of LIG technology represented a remarkable advancement in graphene synthesis [10]. Carbonaceous precursors undergo direct conversion to three-dimensionally porous graphene architectures through a localized photochemical reaction using high-power-density laser pulses. This in situ, bottom-up approach offers several advantages including mask-free patterning, open-air processability, and cost-effectiveness. Consequently, LIG is widely applied in sensors [11, 12], capacitors [13, 14], nanogenerators [15, 16], and catalysis [17, 18] research.

The ultrafast kinetics induced by high-energy-density laser pulses drive sequential precursor processes—e.g., polyimide (PI) dissociation, carbonization, and graphitization—in ambient conditions. Notably, PI molecules are completely ablated at around 700 °C under conventional slow-temperature-rise conditions [19]. However, the ultrafast kinetics also lead to an amorphous and polycrystalline structure in LIG, resulting in compromised electrical properties that limits its application in electronic and electromagnetic devices. Therefore, it is critical to reduce the density of defect and optimize the crystallinity in LIG for tailored devices.

Currently employed strategies for healing defects in graphene involve post-synthesis treatments, including high-temperature heating and chemical reduction. However, these methods fail to heal the defects in patterned LIG. For instance, heating temperature exceeding 1000 °C is usually adopted to obtain reduced graphene oxides with high electrical conductivity, and these experiments need to be conducted under an inert or vacuum atmosphere [20, 21]. However, the treatment cannot be localized to specific regions, causing thermal degradation of the polymeric substrate and damage to patterned LIG. Chemical reduction agents (e.g., hydrazine [22], ethylenediamine [23], ascorbic acid [24]) effectively remove oxygen functionalities, but they cannot induce the lattice reconstruction required for

crystallinity enhancement. Recent advances in 2024 demonstrated millisecond-scale defect mitigation through Joule heating by applying DC voltages to LIG patterns in a vacuum chamber [25]. However, the above mentioned multi-step post-treatments compromise LIG's inherent advantages—single-step patterning and ambient processing capability. Thus, it is challenging to heal the defects in LIG via a facile method.

In this work, we report a designed laser-stepwise-induced graphene (LSIG) method, combining focused and defocused laser processing in a single-step sequence, to optimize crystallinity and sheet resistance of graphene. This design is based on our discovery that focused and defocused laser pulses exhibit significantly distinct effects on morphology and electrical properties of LIG. The initially applied focused laser irradiation leads to longitudinal heat penetration and diffusion through the substrate, enabling conversion of PI molecules into graphene but leaving numerous defects; the subsequently applied defocused laser irradiation effectively heals the defects and increases crystalline domain. Raman spectroscopy confirms crystallinity enhancement: I_D/I_G is reduced from 0.94 to 0.81, and the full width at half maximum (FWHM) of the 2D band narrows from 158.31 cm^{-1} to 100.15 cm^{-1}, indicating improved graphitic ordering. Importantly, the sheet resistance of LSIG is reduced from 25.3 Ω sq^{-1} to 15.0 Ω sq^{-1}. To demonstrate the potential of LSIG for electromagnetic applications and the significance of sheet resistance reduction, a flexible frequency-selective surface (FSS) containing 16 × 16 LSIG square loop units was designed and fabricated. The FSS exhibits an enhanced effective bandwidth of 4.92 GHz and a transmission (T) coefficient of 0.057 at its resonant frequency. Furthermore, the infrared stealth performance of this FSS demonstrates its ability to serve as a multifunctional surface in an integrated system. The development of this single-step patterned and open-air-processable LSIG would advance direct writing of functional films for electronic and electromagnetic devices.

RESULTS AND DISCUSSION

Design of Laser-stepwise Induced Graphene Technology

Compared to conventional heating, laser processing is distinguished by the ultrahigh energy density, delivered on millisecond to femtosecond time scales. This enables PI molecules to be rapidly converted into LIG [25-27], whereas under conventional slow-temperature-rise conditions (ambient), PI molecules are completely ablated at approximately 700 °C [19]. However, the laser-induce ultrafast kinetics often results in incomplete reactions, leaving substantial defects in LIG and compromising its electrical properties. Inspired by reported work on metal laser processing [28, 29], we explored defocused laser scanning—where a larger irradiated area reduces energy density—to moderate the reaction rate. Unexpectedly, this approach instead increased sheet resistance. Consequently, we conducted a one-line focused/defocused laser scan to examine their respective effects on the LIG surface (**Figure 1a**). Notably, focused laser scanning produces a steep cliff along the scan path, due to a photoetching effect caused by elevated temperature and stress. In contrast, defocused laser scanning markedly reduces photoetching, resulting in a flatter surface of reduced thickness. Based on these observations, we designed the LSIG technology (**Figure 1b)**. Initially, focused laser irradiation is intended to vertically penetrate more energy into the PI film, providing the foundation for optimized sheet resistance. The laser-induced ultrafast kinetics and uneven temperature distribution result in large amounts of defects. Subsequently, defocused laser irradiation, is employed to heal the defects and enhance the crystallinity. The entire process can be completed in a single step under ambient conditions, demonstrating versatility and adaptability across multiple disciplines.

Mechanism of the Sheet Resistance Reduction

The sheet resistance of LIGs and LSIGs at varying laser powers is systematically shown in **Figure 2a**. Both samples exhibit a linear inverse correlation between sheet resistance and laser power, as evidenced by the negative slopes of the fitted curves (LIG: −3.34, LSIG: −2.19). Compared with LIG, LSIGs achieve a markedly reduced sheet resistance, with the minimum value of 15.0 Ω sq^{-1} (a 40.7% decrease from 25.3 of LIG). This

result demonstrates that the designed experiment has achieved the expected effect. Furthermore, the morphology, defect structure, and atomic binding states were investigated to determine the mechanism of sheet resistance reduction.

Scanning electron microscopy (SEM) characterization was adopted to investigate the microstructure of LSIG. As shown in **Figure 2b,** the LSIG surface exhibits a grid structure, in which the gully structures are formed by laser-induced photoetching effect. A large amount of flocculent sediment is deposited on the ridges, which were not irradiated by the laser. Thus, these deposits are assumed to be the photoetching byproducts of PI molecules and are expelled from the gullies by released gases. Notably, LIG (**Figure S1**) exhibits similar surface morphology to LSIG, demonstrating the repeated laser processing not damage the surface. To verify the source of gully, we simulated the temperature distribution on the cross section of LIG film (**Figure 2c**). An ultrahigh temperature exceeding 1500 K is generated at the irradiated part of laser pulse, which can lead to ablation of PI and LIG molecules. Importantly, as the distance from the irradiated center increases, the temperature gradually decreases, leading to incomplete chemical reactions and a large number of defects. From these results, it can be demonstrated that the microstructure of LSIG primarily depended on the laser-focused scanning.

To investigate potential defect healing, Raman spectra characterization was employed (**Figure 2d**). The D, G, and 2D peak located at approximately 1342 cm^{-1}, 1575 cm^{-1}, and 2680 cm^{-1} confirm the formation of LIG and LSIG [30, 31]. The D and G peak originate from the breathing mode of C-sp^2 in distorted lattice and the in-plane vibration of C-sp^2 in hexagonal lattice, respectively [32, 33]. The blunt 2D peak can demonstrate the formation of multilayer graphene [34]. For a more detailed analysis, I_D/I_G ratio was calculated (**Figure 2e**), which is an important indicator of defect density on the basal plane or edges of the crystalline domains.. Compared to LIG, the I_D/I_G ratio of LSIG decreases from 0.94 to 0.81, demonstrating reduced degree of defects after defocused laser irradiation. Additionally, crystalline size along the a-axis (L_a) was calculated from I_G/I_D ratio via following equation:

$$L_a = (2.4 \times 10^{-10}) \times \lambda_l^4 \times (I_G/I_D)$$

where λ_l is 532 nm (wavelength of the Raman laser) [35]. The L_a of LSIG reaches 23.7 nm, which is larger than that of LIG (20.4 nm). This implies that the LSIG technique can

effectively heal defects in LIG and promote grain growth, resulting in larger crystalline domains. **Figure 2f** depicts the I_{2D}/I_G ratio and the full width at half maximum (FWHM) of the 2D band, which are indicators of crystalline quality and graphene layer count [36]. The I_{2D}/I_G ratio increases from 0.27 for LIG to 0.36 for LSIG, and the 2D FWHM decreases from 168.31 cm^{-1} to 100.15 cm^{-1}. The results imply reduced stacking and enhanced crystalline quality, suggesting the expansion of graphene layers. In addition, a glue shift of ~10 cm^{-1} of the 2D peak can be observed, which may be caused by several factors, such as in-lattice strain, band structure modulation, and layers changing [37, 38].

X-ray photoelectron spectroscopy (XPS) was further adopted to investigate the elements and bonding states. As depicted in **Figure S2**, both of LIG and LSIG show C 1*s*, O 1*s*, and N 1*s* peak at 284 eV, 531 eV, and 399 eV, respectively. Compared to LIG, the nitrogen content of LSIG increases from 27.41% to 37.65%, likely due to additional nitrogen incorporation from the air during defocused laser irradiation. Simultaneously, the carbon and oxygen contents decreased from 64.19% to 55.19% and from 8.40% to 7.16%, respectively. Detailed analysis on C 1*s* spectrum (**Figure 2g** and **2h**) shows that the content of C−O bonds significantly decreases from 42.09% in LIG to 3.14% in LSIG. These results reveal that the loss of carbon and oxygen atoms is primarily due to the reduction of C–O bonds in LIG, promoted by defocused laser scanning. Notably, the content of C−C bonds increases from 46.2% in LIG to 82.13% in LSIG. This suggests that secondary defocused laser irradiation enhances the PI to graphene reaction completeness.

Chemical and Mechanical Stability

To study the potential of the LSIG in practical application, the chemical and mechanical stabilities were evaluated. The LSIG samples were subjected to four typical environments, including H_2O, 5 wt% NaCl, 0.5 M H_2SO_4, and air at 100℃. Each sample was treated for 72 hours, after which the variation in sheet resistance was measured (**Figure 3a**). The LSIG demonstrates extraordinary stability with variations in sheet resistance below 6.2%. This finding underscores the potential of the LSIG for long-term service in extreme environments. Notably, mechanical stability was investigated via uniaxial repeated tensile testing to simulate tension caused by thermal expansion or stress deformation of equipment

housing, as LSIG is applied as a skin material (**Figure 3b**). The mechanical testing setup and the sample preparation are shown in **Figure S3**, and the maximum tensile strain rate was set as 0.3%. After cyclic test for 1000 seconds, the variation in sheet resistance remained stable. Upon release of the applied strain, the sheet resistance of LSIG fully recovered to its initial value. The demonstrated stability and reliability of LSIG indicate its significant potential for practical applications.

Design of LSIG FSS

The as-prepared LSIG, with its reduced sheet resistance, enables electromagnetic manipulation for selective frequency shielding. **Figure 4a** depicts a schematic of the LSIG FSS comprising a 16 × 16 array of LSIG square-loop units. The geometrical parameters *p*, *q*, and *s* are determined to be 12 mm, 6 mm, and 3 mm, respectively. The design and simulation of the FSS were conducted using CST Microwave Studio. The unit cell structure is simulated with periodic boundary conditions along the x and y axes, while Floquet port excitations are applied along the z direction, both above and below the unit cell. The equivalent circuit model of the FSS is displayed in **Figure 4b**, in which equivalent inductive (L) and capacitive (C) lumped components construct the FSS. **Figures 4c** and **4d** show the *S*-parameters of the LSIG FSS, demonstrating that sheet resistance is a critical factor in determining selective electromagnetic shielding performance. As sheet resistance increase from 15 Ω sq^{-1} to 35 sq^{-1}, the effective bandwidth of S_{21} obviously decrease from 4.92 GHz (at 15 Ω sq^{-1}) and 3.42 (at 20 Ω sq^{-1}) to 0 GHz (at 25–35 sq^{-1}). In addition, S_{11} mainly remains above –10 dB for all sheet resistance values in the 2–20 GHz frequency range, indicating strong reflection loss of the incident wave.

To further explore the electromagnetic shielding mechanism, the power coefficients of *T*, reflection (*R*), and absorption (*A*) were calculated using the following formula:

$$T = |S_{21}|^2,$$

$$R = |S_{11}|^2,$$

$$A = 1 - R - T$$

As shown in **Figure 4e**, *A* generally increases as the frequency rises from 2 GHz to 20 GHz, demonstrating enhanced electromagnetic wave absorption loss. *A* at 2 GHz and 20 GHz

is 0.046 and 0.39, respectively. The variation of *R* reveals that reflection of the incident electromagnetic wave first increases and then decreases. The *T*, *R*, and *A* for the FSS with sheet resistances between 20 and 35 Ω sq^{-1} are shown in **Figure S5**, displaying trend similar to those observed at 15 Ω sq^{-1}. Furthermore, the relationship between transmission coefficient and sheet resistance over 2–20 GHz was simulated (**Figure 4f**). As LIG sheet resistance increases from 15 Ω sq^{-1} to 35 sq^{-1}, the resonant frequency decreases from 11.38 GHz to 10.7 GHz, and the minimum value of *T* increases from 0.057 to 0.15 (**Figure 4g**). These results indicate that increasing sheet resistance weakens selective wave shielding performance, and that the as-prepared LSIG, with its reduced sheet resistance of 15 Ω sq^{-1}, is a promising material for electromagnetic wave manipulation.

To explore the response of the LSIG FSS to incident electromagnetic waves, the surface current and voltage densities were analyzed (**Figure 4h**). At 11.38 GHz, the voltage density decreases from 6.556 × 10^3 V m^{-1} to 5.982 × 10^3 V m^{-1} as sheet resistance increases, and the slight intermediate rise may originate from the combined effects of a 25% increase in sheet resistance (20 Ω sq^{-1} to 25 Ω sq^{-1}) and a 0.73% decrease in current density (27.4 A m^{-1} to 27.2 A m^{-1}). Moreover, as sheet resistance increases, the current density decreases from 33.2 A m^{-1} to 20.6 A m^{-1}, demonstrating resonance weakening of electromagnetic waves. Furthermore, the oblique-incidence performance of the FSS was evaluated for incident angles of 0–40°. As displayed in **Figure 4i**, increasing the incident angle leads to pronounced multiple resonances. A new resonant appears at 17.77 GHz when the incident angle is 27.80° (*T* = 0.1). Simultaneously, the effective bandwidth widens from 4.92 GHz to 5.72 GHz as the incident angle increases from 0° to 23.81°; beyond 23.81°, the effective band splits around its midpoint as the angle increases to 40°. Furthermore, the current density of the FSS (*Rs* = 15 Ω sq^{-1}) was examined to illustrate the varied response for incident angles of 0–40° (**Figure 4j** and **S8**). At 0°, the inner square edges exhibit a symmetrical distribution of high current density. At 30°, the current is mainly concentrated in the left inner square edge and outer square edge, indicating that the oblique incidence has a large impact on the current distribution, which further affects the operating band of FSS.

Experimental Performance Tests of the LSIG FSS

Using LSIG technology, the FSS were fabricated with the advantages of mask-free, single-step patterning, open-air processability, and reagent-free processing (**Figure 5a**). **Figure 5b** demonstrates the excellent flexibility of the LSIG FSS, as evidenced by its ability to be freely rolled. This flexibility is important for practical applications requiring surface conformality. In addition, the remarkable lightweight nature of the LSIG FSS is shown in **Figure 5c**, where it is placed on a branch without noticeable bending. To verify performance of the designed FSS, the selective electromagnetic shielding of the LSIG FSS (Rs = 15 Ω sq^{-1}) was measured. Using the experimental setup depicted in **Figures 5d** and **5e**, electromagnetic shielding measurements were conducted in an anechoic chamber. To investigate shielding performance against normal and oblique incidence, the angle between the wave propagation direction and the specimen's normal was set to 0°, 15°, and 30°. The measured results exhibit excellent agreement with the simulated results (**Figure 5f–h**).

Infrared Stealth Performance of the LSIG FSS

To demonstrate the potential of the prepared LSIG FSS as a multifunctional surface, we investigated its infrared (IR) stealth performance, which is critical for safeguarding electronic instruments against thermal detection [39, 40]. As shown in **Figure 6**, the stealth performance for targets with temperatures ranging from ~37 °C (body temperature) to 200 °C was tested. The FSS, consisting of a 16 × 16 array, was placed in front of a volunteer's body and in front of a bucket of hot water (**Figures 6a** and **6b**). IR imaging analysis revealed that the FSS effectively attenuates the infrared radiation emitted by the heat source, rendering the shielded area visually indistinguishable from the background in the thermal image. Furthermore, an FSS unit was placed on a ceramic plate heater for continuous monitoring over 900 s, with the heater temperature set to 75 °C (**Figure 6b**) and 150 °C (**Figure 6c**). The detected temperature on the outer square loop decreased from 75 °C to 59.7 °C and from 150 °C to 111.8 °C. The detected temperature on the inner square decreased from 75 °C to 65.7 °C and from 150 °C to 122.8 °C. The difference in temperature between the outer loop and the inner square can be explained by the porous architecture and low thermal conductivity of LSIG, which together impede heat transfer from the lower surface to the upper surface. **Figure 6d** displays the temperature change over 900 s when the heater is set to 150 °C. This

demonstrates that the surface temperature rises rapidly and then stabilizes, indicating long-term stability for IR stealth.

CONCLUSIONS

This work presents an LSIG technology that heals defects and promotes crystalline domain growth in LIG, thereby reducing its sheet resistance for electromagnetic applications. Compared to LIG, the I_D/I_G ratio of LSIG decreases from 0.94 to 0.81, and the 2D FWHM narrowed from 158.31 cm^{-1} to 100.15 cm^{-1}, resulting in a reduction of sheet resistance from 25.3 Ω sq^{-1} to 15.0 Ω sq^{-1}. A FSS for electromagnetic wave manipulation was designed and fabricated, exhibiting an enhanced effective bandwidth of 4.92 GHz and a T coefficient of 0.057 at its resonant frequency. Furthermore, the infrared stealth performance demonstrates the potential of the LSIG FSS as a multifunctional surface in next-generation integrated systems. The development of this single-step, open-air–processable, mask-free LSIG technology provides a critical pathway for direct writing of functional films.

MATERIALS

The PI film with the thickness of 150 am was purchased from Zhuzhou Times New Materials Technology Co., Ltd. (China). The PI film was adsorbed on the laser platform through negative pressure and scanned by an infrared laser (Proteases S, LPKF, Germany) to fabricate LIG with the focus height set to 150 μm. In the LSIG process, the initial laser scan is identical to the LIG fabrication protocol; the focus height is then adjusted to 2 mm for defocused laser scanning. The fabrication of LIG and LSIG were carried out under atmospheric conditions at 26°C and 45% relative humidity. The wavelength of the laser generated by the laser source is 1064 nm.

CHARACTERIZATION

The surface morphology of the sample was characterized using a scanning electron microscope (JSM-7610F Plus). Raman spectra were characterized with a Raman spectrometer (LabRam HR Evolution). The sheet resistance was measured using a 4-Point Probes Resistivity Measurement System (RTS-8) for eliminate the influence of contact

resistance on results. Hyper-depth of field three-dimensional microscopic system (VHX-600E) was adopted to capture high-definition images of surface topography. XPS data were collected with a Scanning X-ray Microprobe (ESCALAB 250Xi). The mechanical stability of LSIG was tested using a mechanical testing machine (Instron-5848) for repeatedly applying 0.3% uniaxial tensile strain, and the data was collected by a digital multimeter (Keithely-6510). Infrared images were captured using an infrared camera (ST9450). Experimental measurement of the electromagnetic shielding performance for LSIG FSS was carried in an anechoic chamber, in which the FSS was placed between the receiving antenna and transmitting antenna.

REFERENCES

[1] Novoselov, K. S.; Fal′ko, V. I.; Colombo, L.; Gellert, P. R.; Schwab, M. G.; Kim, K. A roadmap for graphene. *Nature* **2012**, *490*, 192-200.

[2] Weiss, N. O.; Zhou, H.; Liao, L.; Liu, Y.; Jiang, S.; Huang, Y.; Duan, X. Graphene: An emerging electronic material. *Adv. Mater.* **2012**, *24*, 5782-5825.

[3] Geim, A. K.; Novoselov, K. S. The rise of graphene. *Nat. Mater.* **2007**, *6*, 183-191.

[4] Zhang, Y.; Zhang, L.; Zhou, C. Review of chemical vapor deposition of graphene and related applications. *Acc. Chem. Res.* **2013**, *46*, 2329-2339.

[5] Yu, Q.; Lian, J.; Siriponglert, S.; Li, H.; Chen, Y. P.; Pei, S.-S. Graphene segregated on ni surfaces and transferred to insulators. *Appl. Phys. Lett.* **2008**, *93*, 113103.

[6] Coleman, J. N.; Lotya, M.; O'Neill, A.; Bergin, S. D.; King, P. J.; Khan, U.; Young, K.; Gaucher, A.; De, S.; Smith, R. J.; Shvets, I. V.; Arora, S. K.; Stanton, G.; Kim, H.-Y.; Lee, K.; Kim, G. T.; Duesberg, G. S.; Hallam, T.; Boland, J. J.; Wang, J. J.; Donegan, J. F.; Grunlan, J. C.; Moriarty, G.; Shmeliov, A.; Nicholls, R. J.; Perkins, J. M.; Grieveson, E. M.; Theuwissen, K.; McComb, D. W.; Nellist, P. D.; Nicolosi, V. Two-dimensional nanosheets produced by liquid exfoliation of layered materials. *Science* **2011**, *331*, 568-571.

[7] Ciesielski, A.; Samorì, P. Graphene via sonication assisted liquid-phase exfoliation. *Chem. Soc. Rev.* **2014**, *43*, 381-398.

[8] Yang, W.; Chen, G.; Shi, Z.; Liu, C.-C.; Zhang, L.; Xie, G.; Cheng, M.; Wang, D.; Yang, R.; Shi, D.; Watanabe, K.; Taniguchi, T.; Yao, Y.; Zhang, Y.; Zhang, G. Epitaxial growth of single-domain graphene on hexagonal boron nitride. *Nat. Mater.* **2013**, *12*, 792-797.

[9] Park, J.; Mitchel, W. C.; Grazulis, L.; Smith, H. E.; Eyink, K. G.; Boeckl, J. J.; Tomich, D. H.; Pacley, S. D.; Hoelscher, J. E. Epitaxial graphene growth by carbon molecular beam epitaxy (CMBE). *Adv. Mater.* **2010**, *22*, 4140-4145.

[10] Lin, J.; Peng, Z.; Liu, Y.; Ruiz-Zepeda, F.; Ye, R.; Samuel, E. L. G.; Yacaman, M. J.; Yakobson, B. I.; Tour, J. M. Laser-induced porous graphene films from commercial polymers. *Nat. Commun.* **2014**, *5*, 5714.

[11] Huang, L.; Liu, Y.; Li, G.; Song, Y.; Su, J.; Cheng, L.; Guo, W.; Zhao, G.; Shen, H.; Yan, Z.; Tang, B. Z.; Ye, R. Ultrasensitive, fast-responsive, directional airflow sensing by bioinspired suspended graphene fibers. *Nano Lett.* **2023**, *23*, 597-605.

[12] Yang, Y.; Song, Y.; Bo, X.; Min, J.; Pak, O. S.; Zhu, L.; Wang, M.; Tu, J.; Kogan, A.; Zhang, H.; Hsiai, T. K.; Li, Z.; Gao, W. A laser-engraved wearable sensor for sensitive detection of uric acid and tyrosine in sweat. *Nat. Biotechnol.* **2020**, *38*, 217-224.

[13] Peng, Z.; Ye, R.; Mann, J. A.; Zakhidov, D.; Li, Y.; Smalley, P. R.; Lin, J.; Tour, J. M. Flexible boron-doped laser-induced graphene microsupercapacitors. *ACS Nano* **2015**, *9*, 5868-5875.

[14] Le, T. S. D.; Lee, Y. A.; Nam, H. K.; Jang, K. Y.; Yang, D.; Kim, B.; Yim, K.; Kim, S. W.; Yoon, H.; Kim, Y. J. Green flexible graphene–inorganic‐hybrid micro‐supercapacitors made of fallen leaves enabled by ultrafast laser pulses. *Adv. Funct. Mater.* **2021**, *32*, 2107768.

[15] Chen, Y.; Xie, B.; Long, J.; Kuang, Y.; Chen, X.; Hou, M.; Gao, J.; Zhou, S.; Fan, B.; He, Y.; Zhang, Y. T.; Wong, C. P.; Wang, Z.; Zhao, N. Interfacial laser‐induced graphene enabling high‐performance liquid-solid triboelectric nanogenerator. *Adv. Mater.* **2021**, *33*, 2104290.

[16] Yang, W.; Han, M.; Liu, F.; Wang, D.; Gao, Y.; Wang, G.; Ding, X.; Luo, S. Structure-foldable and performance-tailorable PI paper-based triboelectric nanogenerators processed and controlled by laser-induced graphene. *Adv. Sci.* **2024**, *11*, 2310017.

[17] Huang, L.; Cheng, L.; Ma, T.; Zhang, J.-J.; Wu, H.; Su, J.; Song, Y.; Zhu, H.; Liu, Q.; Zhu, M.; Zeng, Z.; He, Q.; Tse, M.-K.; Yang, D.-t.; Yakobson, B. I.; Tang, B. Z.; Ren, Y.; Ye, R. Direct synthesis of ammonia from nitrate on amorphous graphene with near 100% efficiency. *Adv. Mater.* **2023**, *35*, 2211856.

[18] Cheng, L.; Ma, T.; Zhang, B.; Huang, L.; Guo, W.; Hu, F.; Zhu, H.; Wang, Z.; Zheng, T.; Yang, D.-T.; Siu, C.-K.; Liu, Q.; Ren, Y.; Xia, C.; Tang, B. Z.; Ye, R. Steering the topological defects in amorphous laser-induced graphene for direct nitrate-to-ammonia electroreduction. *ACS Catal.* **2022**, *12*, 11639-11650.

[19] Ramgobin, A.; Fontaine, G.; Bourbigot, S. Oxygen concentration and modeling thermal decomposition of a high-performance material: A case study of polyimide (Cirlex). *Polym. Adv. Technol.* **2021**, *32*, 54-66.

[20] Vallés, C.; David Núñez, J.; Benito, A. M.; Maser, W. K. Flexible conductive graphene paper obtained by direct and gentle annealing of graphene oxide paper. *Carbon* **2012**, *50*, 835-844.

[21] Grimm, S.; Schweiger, M.; Eigler, S.; Zaumseil, J. High-quality reduced graphene oxide by cvd-assisted annealing. *J. Phys. Chem. C* **2016**, *120*, 3036-3041.

[22] Stankovich, S.; Dikin, D. A.; Piner, R. D.; Kohlhaas, K. A.; Kleinhammes, A.; Jia, Y.; Wu, Y.; Nguyen, S. T.; Ruoff, R. S. Synthesis of graphene-based nanosheets via chemical reduction of exfoliated graphite oxide. *Carbon* **2007**, *45*, 1558-1565.

[23] Samadaei, F.; Salami-Kalajahi, M.; Roghani-Mamaqani, H.; Banaei, M. A structural study on ethylenediamine- and poly(amidoamine)-functionalized graphene oxide: Simultaneous reduction, functionalization, and formation of 3D structure. *RSC Adv.* **2015**, *5*, 71835-71843.

[24] Pan, Z.; Wu, Y.; Yuan, H.; Tang, R.; Ji, L.; Zhou, B.; Ye, C.; Zhang, D.; Qu, Y.; Ji, H.; Zhu, Y. Ascorbic acid-assisted defect healing and stack ordering of graphene films towards high power thermal dispersion. *Carbon* **2021**, *182*, 799-805.

[25] Cheng, L.; Yeung, C. S.; Huang, L.; Ye, G.; Yan, J.; Li, W.; Yiu, C.; Chen, F.-R.; Shen, H.; Tang, B. Z.; Ren, Y.; Yu, X.; Ye, R. Flash healing of laser-induced graphene. *Nat. Commun.* **2024**, *15*, 2925.

[26] Inagaki, M.; Harada, S.; Sato, T.; Nakajima, T.; Horino, Y.; Morita, K. Carbonization of polyimide film "Kapton". *Carbon* **1989**, *27*, 253-257.

[27] Schuepfer, D. B.; Badaczewski, F.; Guerra-Castro, J. M.; Hofmann, D. M.; Heiliger, C.; Smarsly, B.; Klar, P. J. Assessing the structural properties of graphitic and non-graphitic carbons by Raman spectroscopy. *Carbon* **2020**, *161*, 359-372.

[28] Bernstein, J. B.; Joo-Han, L.; Gang, Y.; Dahmas, T. A. Analysis of laser metal-cut energy process window. *IEEE Trans. Semicond. Manuf.* **2000**, *13*, 228-234.

[29] Dutta Majumdar, J.; and Manna, I. Laser material processing. *Int. Mater. Rev.* **2011**, *56*, 341-388.

[30] Chen, Y.; Lu, X.; Ma, G.; Kim, M.; Yu, R.; Zhong, H.; Chan, Y. H. T.; Tan, M.; Liu, Y.; Li, M. G. One-step laser-guided fabrication of 3D self-assembled graphene micro-rolls. *ACS Nano* **2025**, *19*, 5769–5780.

[31] Chen, Y.; Guo, Y.; Xie, B.; Jin, F.; Ma, L.; Zhang, H.; Li, Y.; Chen, X.; Hou, M.; Gao, J.; Liu, H.; Lu, Y.-J.; Wong, C.-P.; Zhao, N. Lightweight and drift-free magnetically actuated millirobots via asymmetric laser-induced graphene. *Nat. Commun.* **2024**, *15*.

[32] Ferrari, A. C.; Meyer, J. C.; Scardaci, V.; Casiraghi, C.; Lazzeri, M.; Mauri, F.; Piscanec, S.; Jiang, D.; Novoselov, K. S.; Roth, S.; Geim, A. K. Raman spectrum of graphene and graphene layers. *Phys. Rev. Lett.* **2006**, *97*, 187401.

[33] Ferrari, A. C.; Basko, D. M. Raman spectroscopy as a versatile tool for studying the properties of graphene. *Nat. Nanotechnol.* **2013**, *8*, 235-246.

[34] Li, Q. Q.; Zhang, X.; Han, W. P.; Lu, Y.; Shi, W.; Wu, J. B.; Tan, P. H. Raman spectroscopy at the edges of multilayer graphene. *Carbon* **2015**, *85*, 221-224.

[35] Cançado, L. G.; Takai, K.; Enoki, T.; Endo, M.; Kim, Y. A.; Mizusaki, H.; Jorio, A.; Coelho, L. N.; Magalhães-Paniago, R.; Pimenta, M. A. General equation for the determination of the crystallite size La of nanographite by Raman spectroscopy. *Appl. Phys. Lett.* **2006**, *88*, 163106.

[36] Yan, Z.; Liu, Y.; Ju, L.; Peng, Z.; Lin, J.; Wang, G.; Zhou, H.; Xiang, C.; Samuel, E. L. G.; Kittrell, C. Large hexagonal bi‐ and trilayer graphene single crystals with varied interlayer rotations. *Angew. Chem.* **2014**, *126*, 1591-1595.

[37] Ni, Z. H.; Wang, H. M.; Luo, Z. Q.; Wang, Y. Y.; Yu, T.; Wu, Y. H.; Shen, Z. X. The effect of vacuum annealing on graphene. *J. Raman Spectrosc.* **2010**, *41*, 479-483.

[38] Ni, Z. H.; Yu, T.; Lu, Y. H.; Wang, Y. Y.; Feng, Y. P.; Shen, Z. X. Uniaxial strain on graphene: Raman spectroscopy study and band-gap opening. *ACS Nano* **2008**, *2*, 2301-2305.

[39] Li, Y.; Wang, Y.; Li, Z.; Ma, S.; Zhang, Y.; Fan, F.; Huang, Y. Meter-scale wearable multifunctional core-shell nanofiber textiles for ultra-broadband electromagnetic interference shielding and infrared stealth. *Adv. Mater.* **2025**, *37*, 2501485.

[40] Zhao, M.; Zhu, H.; Qin, B.; Zhu, R.; Zhang, J.; Ghosh, P.; Wang, Z.; Qiu, M.; Li, Q. High-temperature stealth across multi-infrared and microwave bands with efficient radiative thermal management. *Nano-Micro Lett.* **2025**, *17*, 199.

ACKNOWLEDGEMENTS

Funding: This work was supported by the National Natural Science Foundation of China (22279097, 62401413, 92163208), the Key R&D Program of Hubei Province (2023BAB103), the Foundation of National Key Laboratory of Microwave Imaging Technology, Natural Science Foundation of Hubei Province (2025AFB038, 2025AFD120), and the Fundamental Research Funds for the Central Universities (WUT: 2024IVA031).

Author contributions: P.C., Y.X., H.Z., and D.H. designed the experiments. P.C., X.Y., H.F., and Y.C. carried out the preparation of LIG and LSIG. X.Y., Y.C., Z.C., W.Q., and Y.L. conducted the characterization of structure, composition and morphology. P.C. and Y.X. conducted the electromagnetic test. Y.X. and W.X. conducted CST simulation and analysis. P.C., Y.X., and R.L. collectively wrote the paper. All authors commented on the final manuscript.

Competing interests: Authors declare that they have no competing interests.

Data and materials availability: All data are available in the main text or the supplementary materials.

TOC

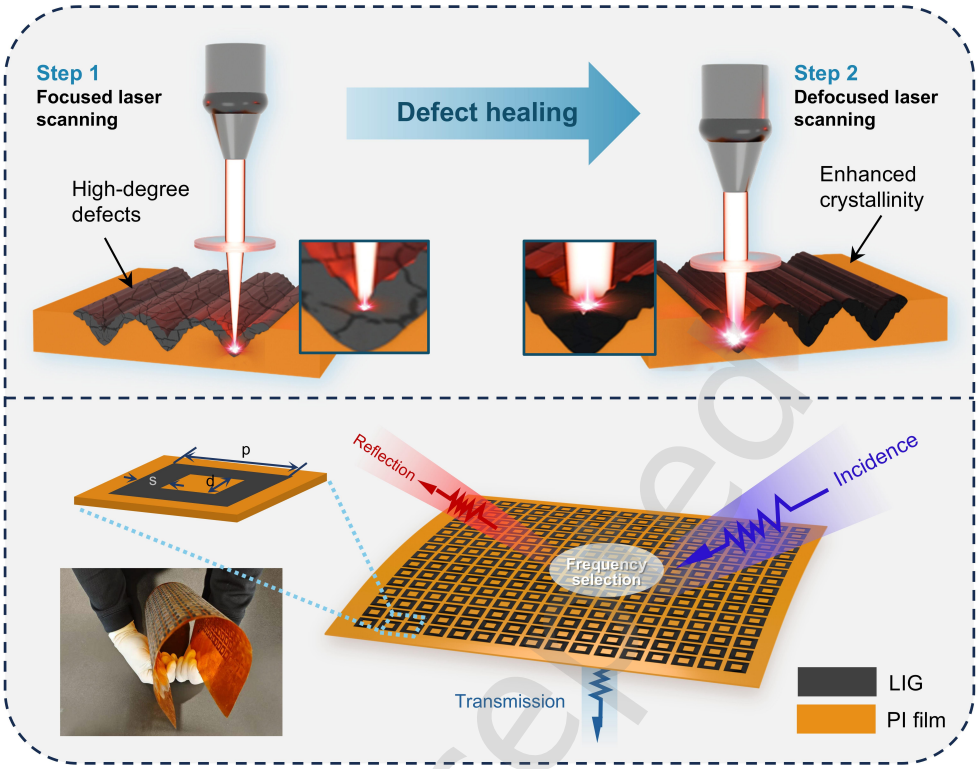

This work develops a laser-stepwise-induced graphene (LSIG) method that heals defects and promotes crystalline domain growth in laser-induced graphene (LIG). LSIG with reduced sheet resistance of 15 Ω sq^{-1} enables direct patterning of a flexible frequency-selective surface for electromagnetic wave manipulation, exhibiting an enhanced effective bandwidth of 4.92 GHz and a transmission coefficient of 0.057 at its resonant frequency.

FIGURES

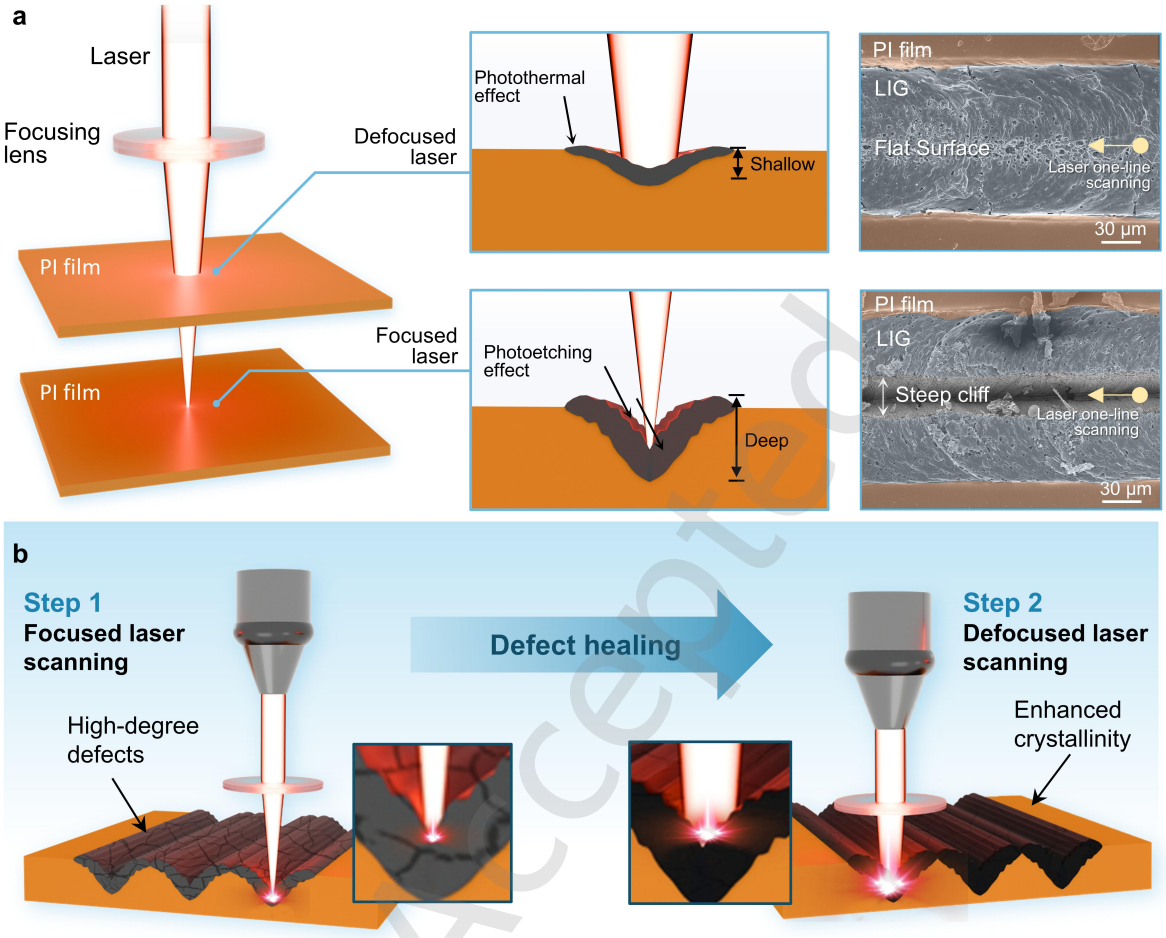

Figure 1. Concept of experimental design.
a Schematic illustration of the difference between focused and defocused laser irradiation.
b Designed LSIG method for reducing sheet resistance of LIG.

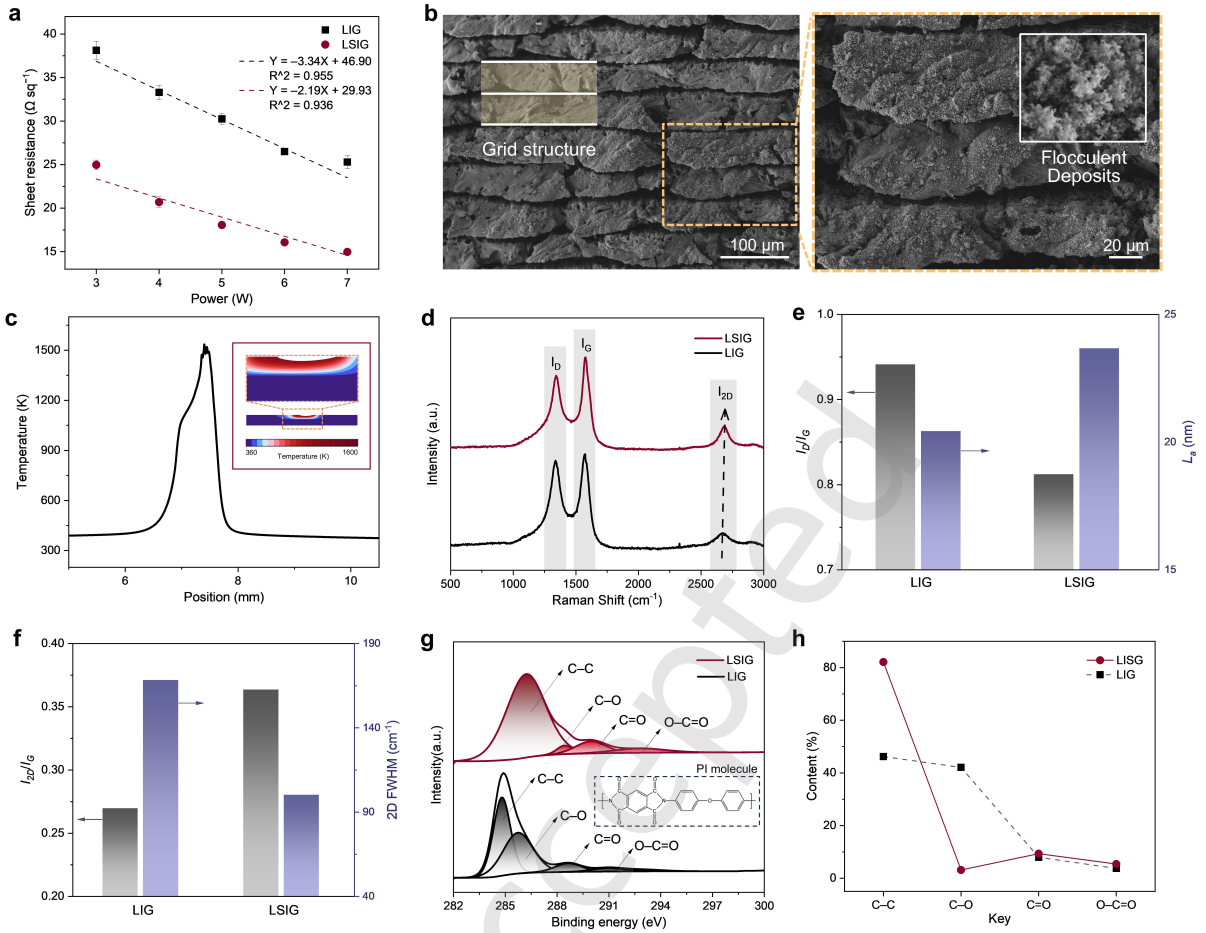

Figure 2. Morphology and defect structure characterization of LSIG.
a Sheet resistance of LIG and LSIG fabricated under various laser powers.
b SEM images of LSIG-7 W surface at different magnification.
c Laser induced temperature distribution on the surface.
d Raman spectra, (**e**) I_D/I_G and corresponding L_a, (**f**) I_{2D}/I_G and 2D band FWHM, (**g**) C 1*s* spectra, and (**h**) key contents of LIG-7 W and LSIG-7 W.

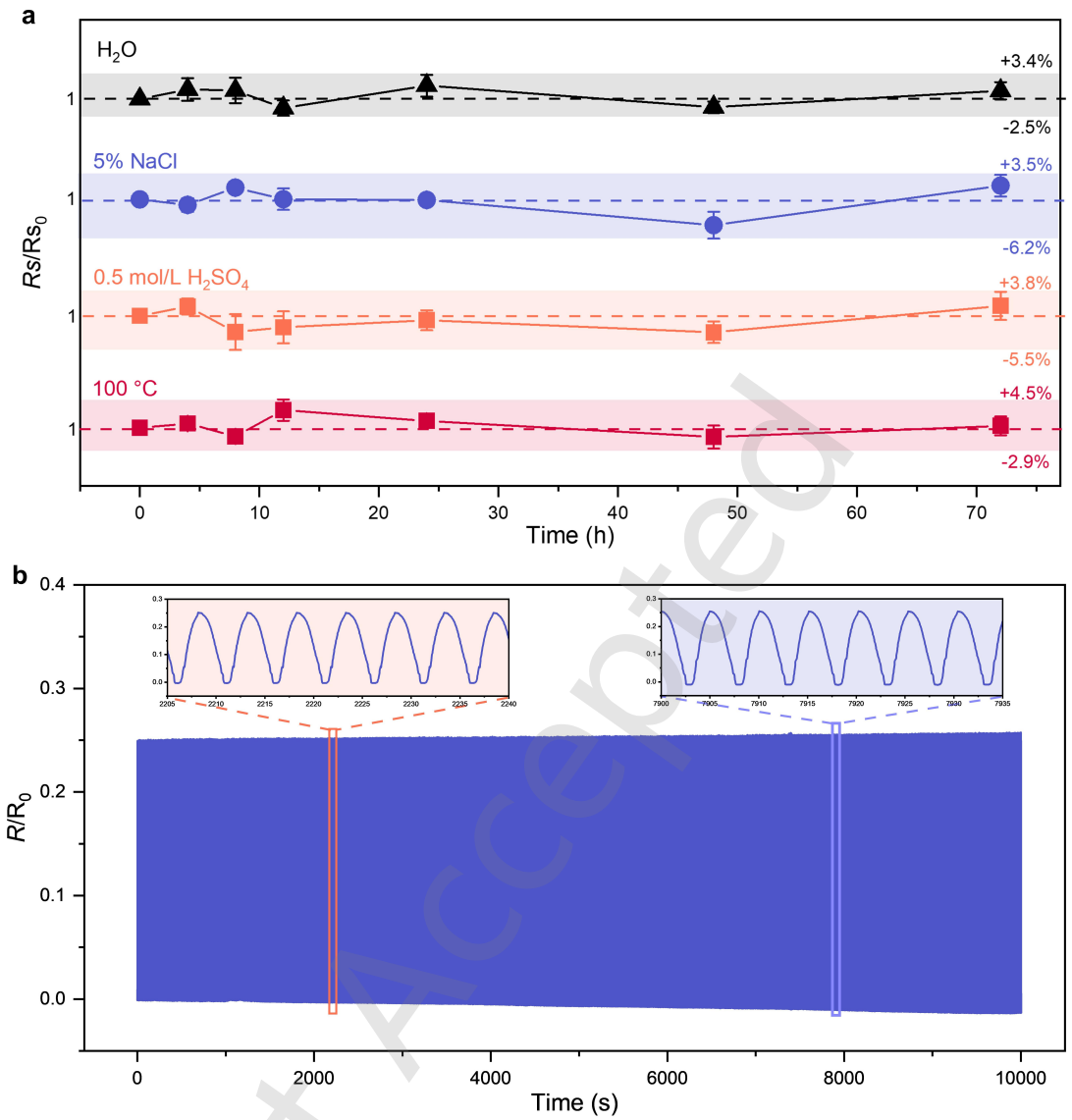

Figure 3. Chemical and mechanical stability of LSIG.

a The change rate of sheet resistance (Rs/Rs_0) under conditions of H_2O, NaCl, H_2SO_4, and 100 ℃.

b The change rate of resistance (R/R_0) under tensile cycle test.

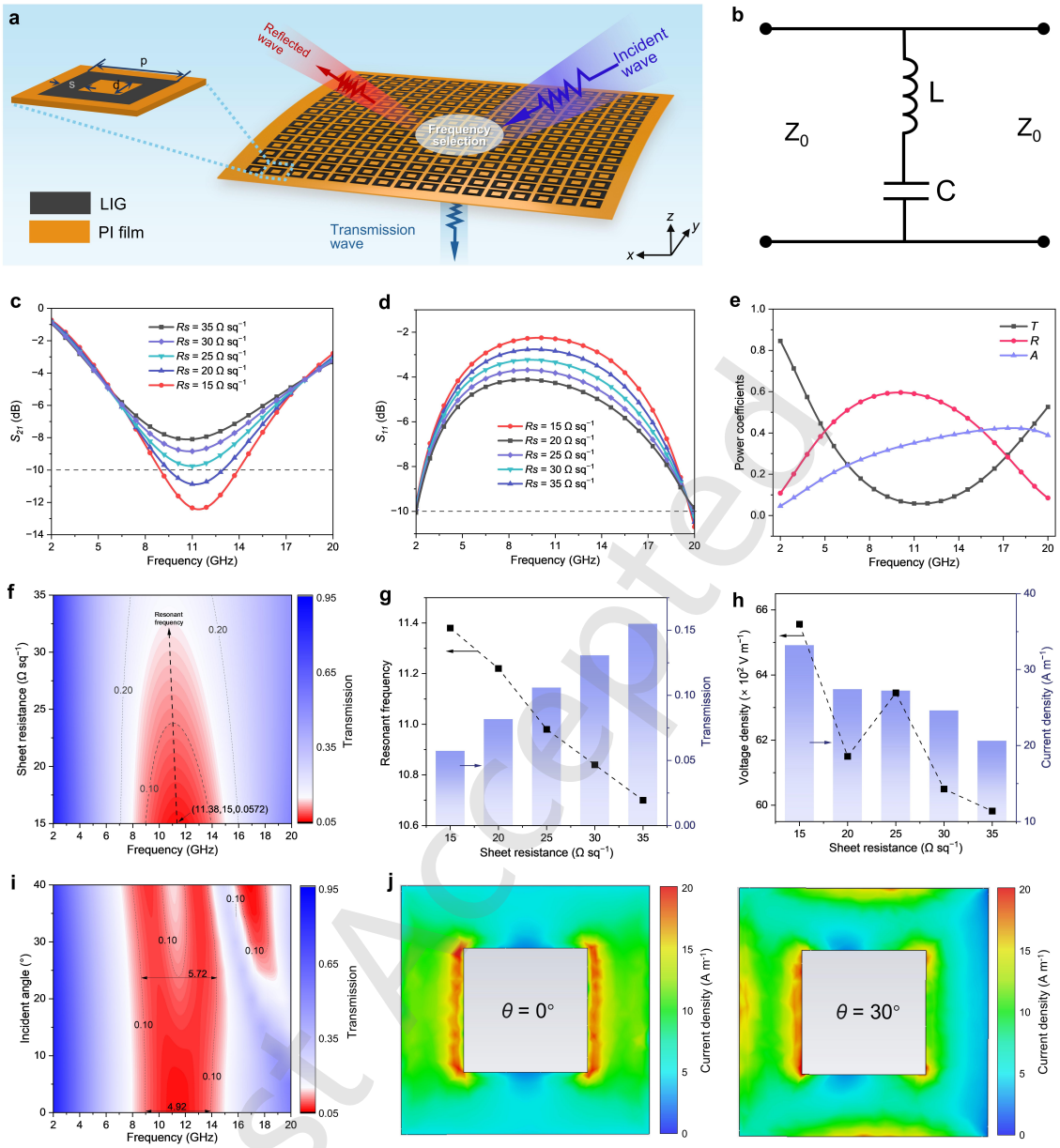

Figure 4. The design of LSIG FSS.

a Schematic showing the geometry and function of the designed LSIG FSS.

b Equivalent circuit of the LSIG FSS.

c and d Simulated S_{21} (**c**) and S_{11} coefficient (**d**) of FSS based on LIGs with various sheet resistance.

e Power coefficients of *T*, *R*, and *A* for LSIG FSS (Rs = 15 Ω sq^{-1}).

f Dependence of *T* coefficient on the sheet resistance at 2–20 GHz.

g Resonant frequency and corresponding *T* coefficient of FSS based on LIGs with various sheet resistance.

h Maximum current density and voltage density at 11.42 GHz of FSS based on LIGs with various sheet resistance.

i Dependence of transmission coefficient at 2–20 GHz on incident electromagnetic wave angles.

j Current density of LSIG FSS (*Rs* = 15 Ω sq^{-1}) at 11.42 GHz under incident electromagnetic wave angles of 0° and 30°.

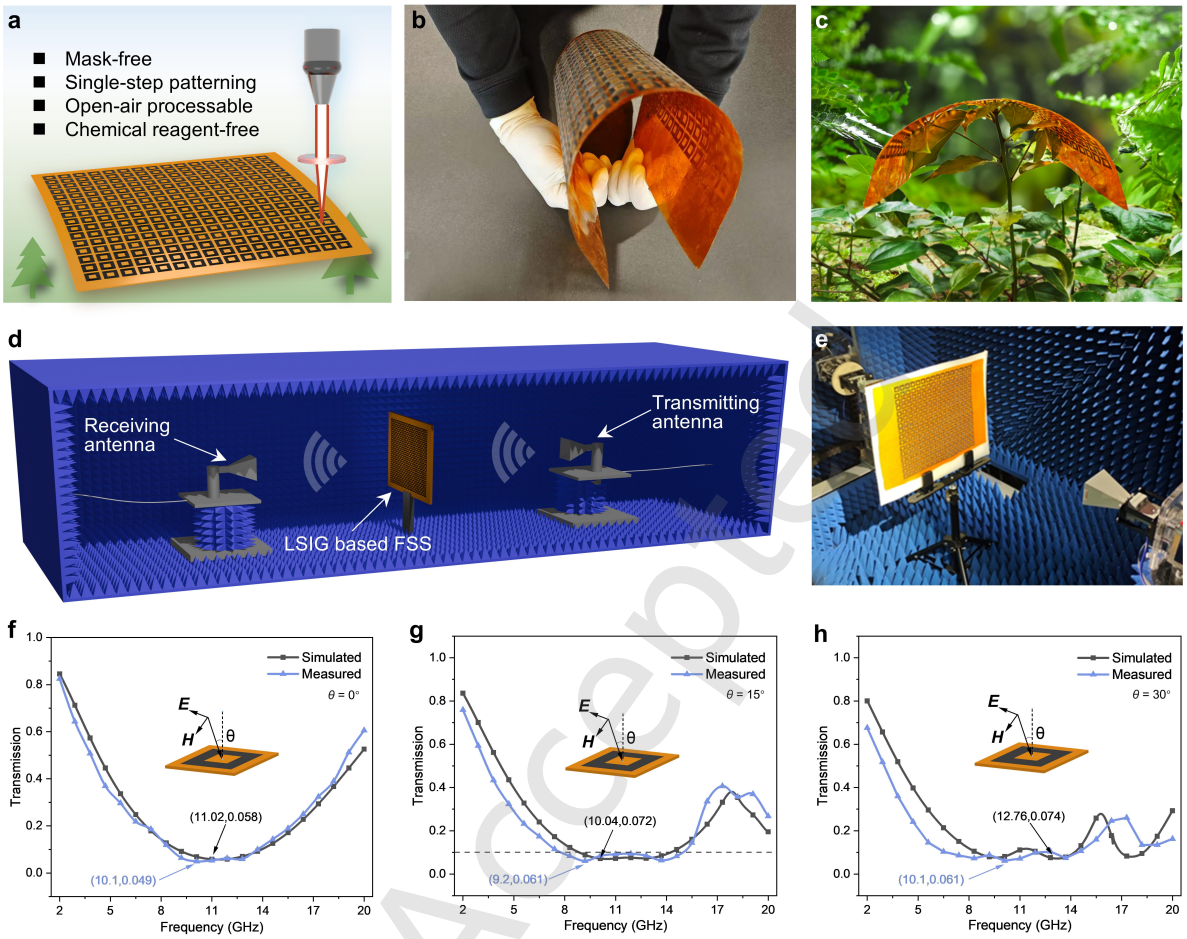

Figure 5. Experimental performance tests of LSIG FSS.

a–c Schematic showing the advantages of LSIG technology (**a**), flexible (**b**) and light (**c**) characteristics of fabricated LSIG FSS.

d and e Schematic (**d**) and photograph (**e**) of measurement environment.

f–h Measured and simulated *T* coefficient of LSIG FSS (*Rs* = 15 Ω sq^{-1}).

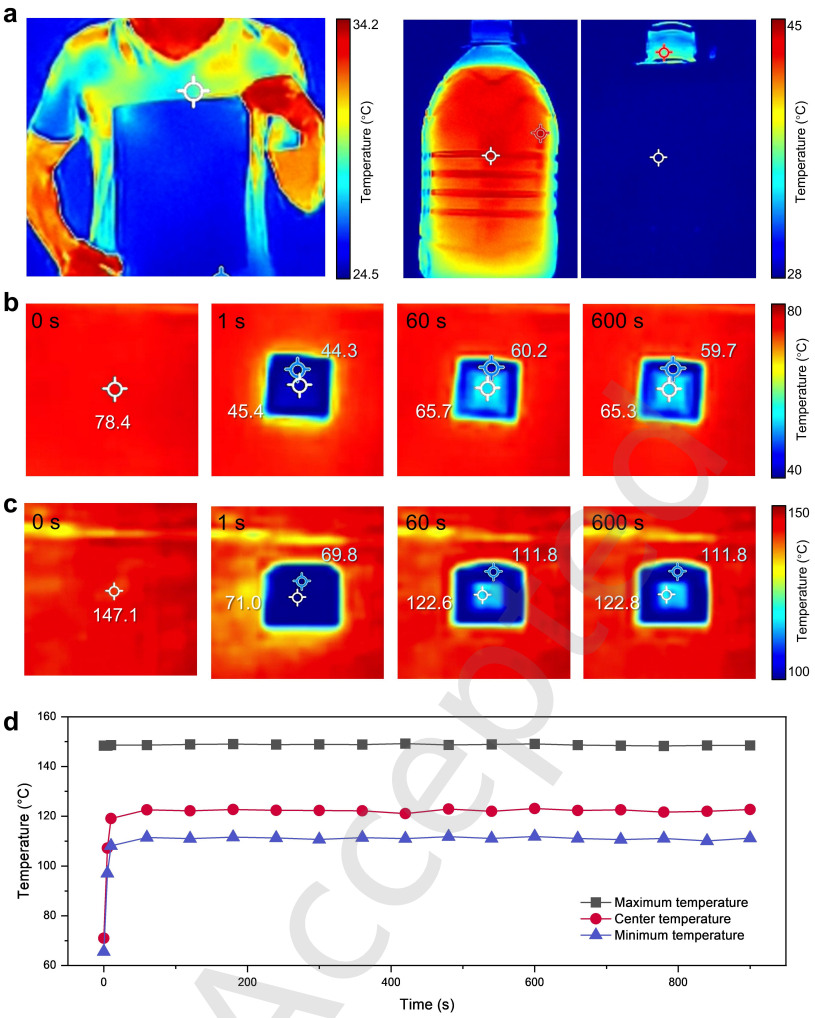

Figure 6. IR stealth performance of LSIG FSS.

a IR images of the LSIG FSS held in front of a volunteer's body and a bucket of hot water.

b and c IR images of the LSIG FSS unit placed on heating stages with the temperature set to 75°C (**b**) and 150°C (**c**).

d Variation in the maximum, minimum, and center temperatures detected in (**c**) at different heating times.

Electronic Supplementary Material

Laser-stepwise-induced graphene with reduced sheet resistance enables electromagnetic shielding manipulation

Pengfei Chen[1,2], Yitong Xin[2,3], Haoran Zu[2,3], Xinrui Yang[1,2,4], Hao Feng[2,4], Wenxiang Xu[2], Yifan Chang[1,2], Zibo Chen[1,2], Wei Qian[2], Yong Lv[5], Huaqiang Fu[1,2]✉, Lin Ren[6], and Daping He[1,2,4]✉

[1] School of Materials Science and Engineering, Wuhan University of Technology, Wuhan 430070, China
[2] Hubei Engineering Research Center of Radio Frequency Microwave Technology and Application, School of Physics and Mechanics, Wuhan University of Technology, Wuhan 430070, China
[3] School of Information Engineering, Wuhan University of Technology, Wuhan 430070, China
[4] State Key Laboratory of Silicate Materials for Architectures, Wuhan University of Technology, Wuhan 430070, China
[5] Hubei Key Laboratory of Theory and Application of Advanced Material Mechanics, School of Physics and Mechanics, Wu Daping He *han University of Technology, Wuhan 430070, China*
[6] Hubei Longzhong Laboratory, Wuhan University of Technology Xiangyang Demonstration Zone, Xiangyang 441000, China

*Address correspondence to Huaqiang Fu, fuhuaqiang@whut.edu.cn; Daping He, hedaping@whut.edu.cn

Supporting information to https://doi.org/10.26599/NR.2025.94908018

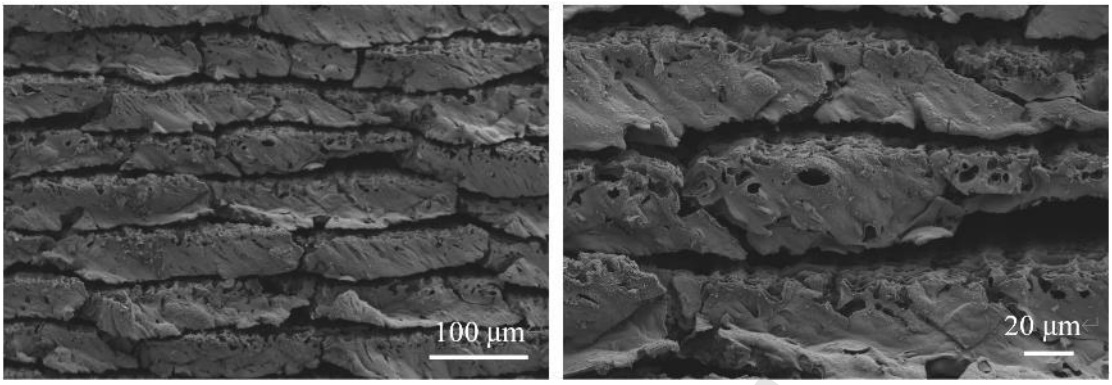

Figure S1. SEM images of LIG-7 W surface at different magnification.

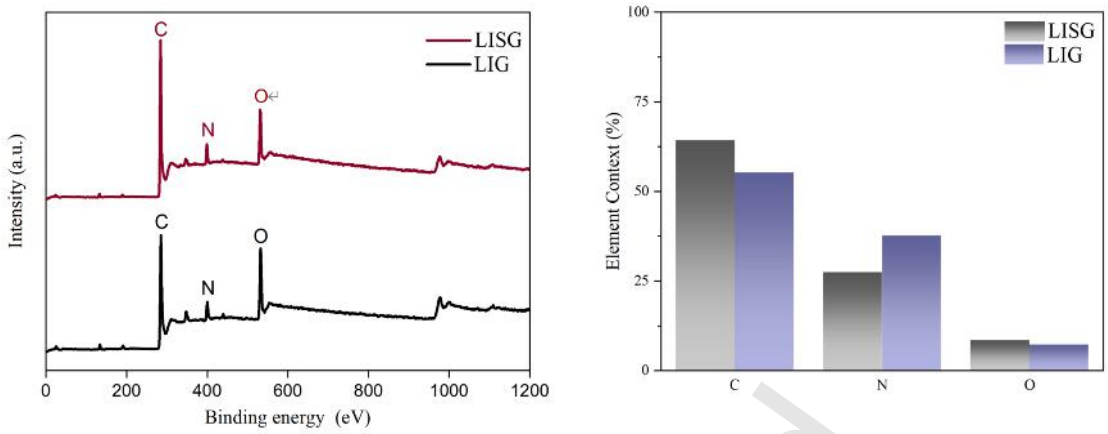

Figure S2. X-ray photoelectron spectroscopy (XPS) and analyzed element content.

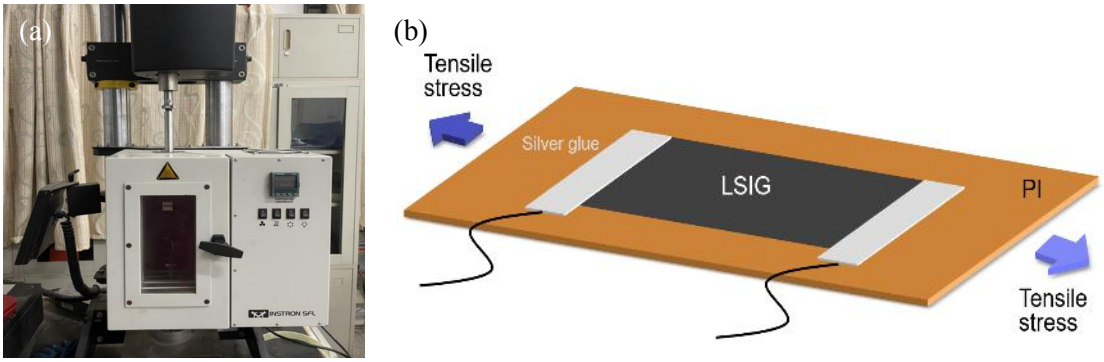

Figure S3. (a) Photograph of the mechanical test. (b) Schematic of the prepared sample for mechanical test.

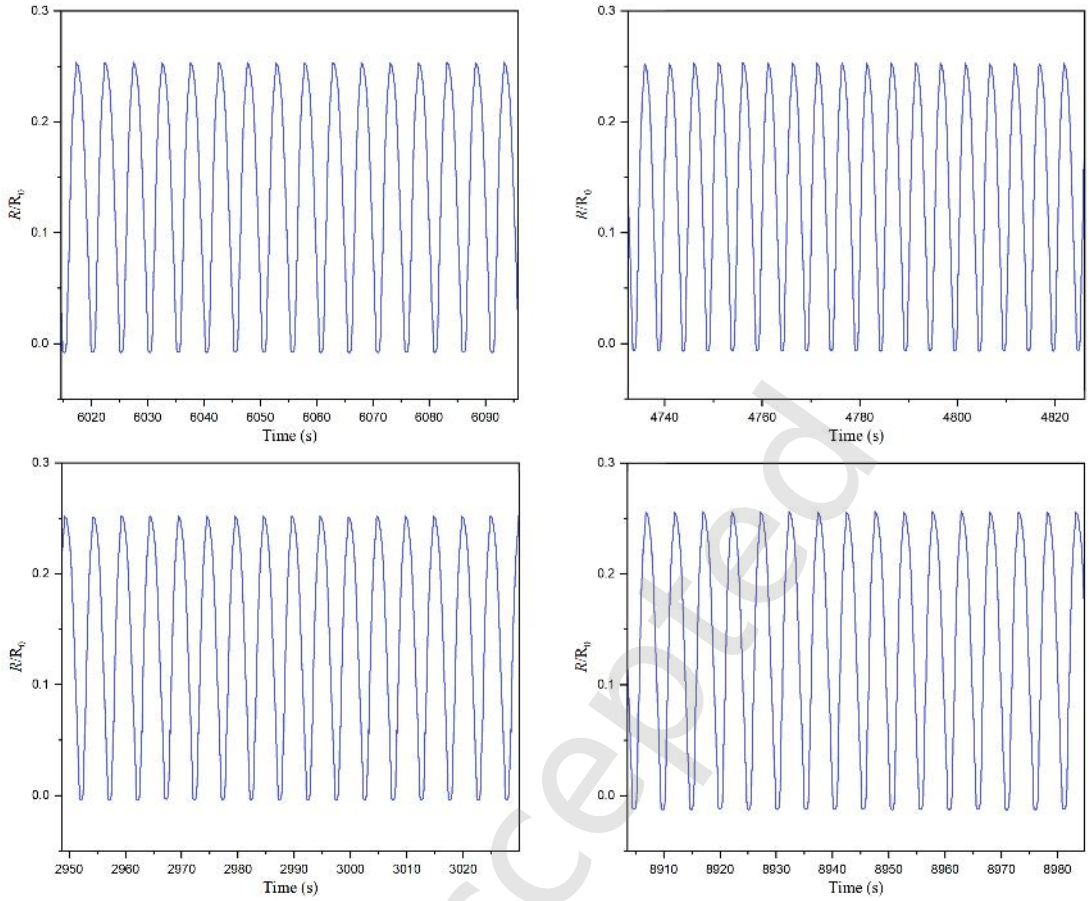

Figure S4. The change rate of resistance (R/R_0) under tensile cycle test.

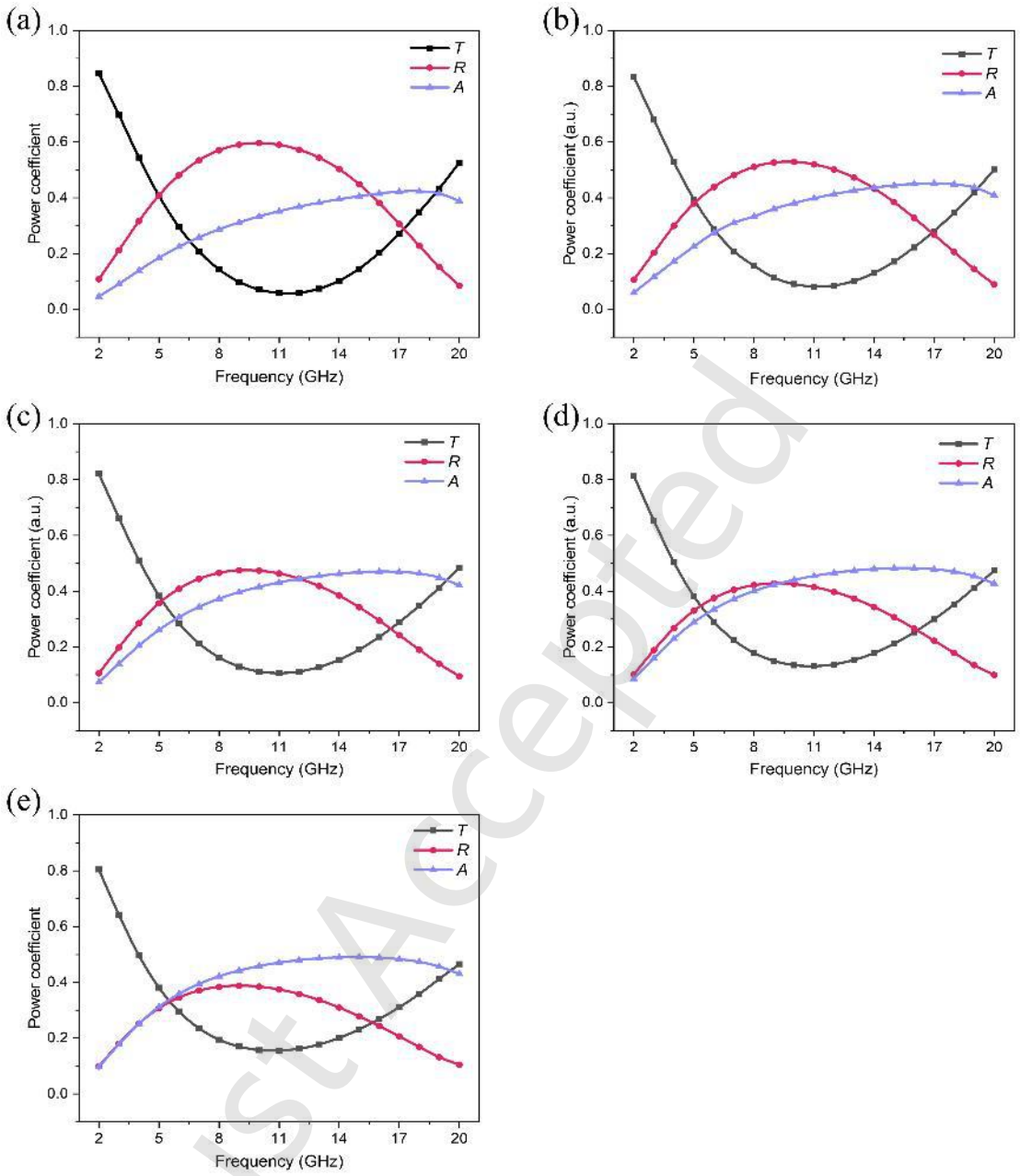

Figure S5. Power coefficients of *T*, *R*, and *A* of the FSS with the sheet resistance of 15 Ω sq^{-1} (a), 20 Ω sq^{-1} (b), 25 Ω sq^{-1} (c), 30 Ω sq^{-1} (d), and 35 Ω sq^{-1} FSS (e).

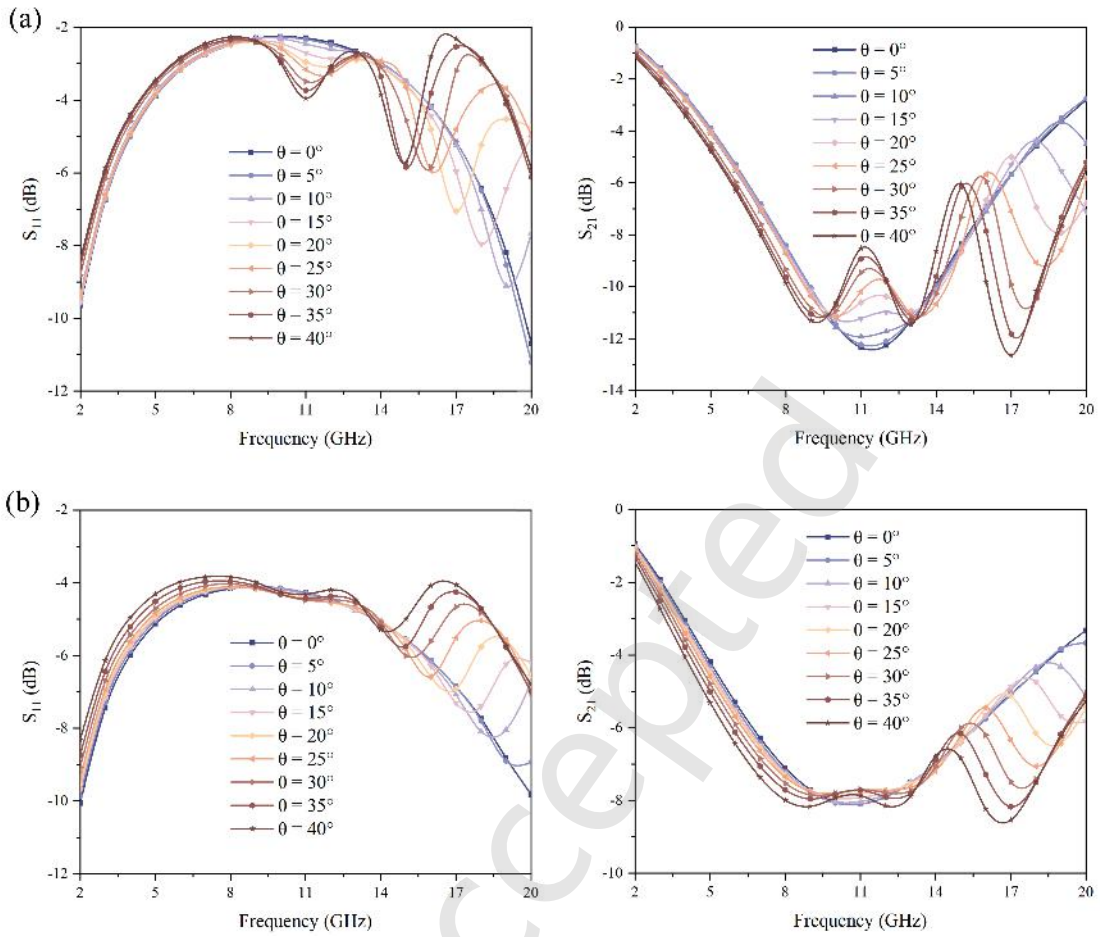

Figure S6. Simulated S_{21} and S_{11} of the FSS with the sheet resistance of 15 Ω sq^{-1} (a) and 35Ω sq^{-1} (b) under incident electromagnetic wave angles from 0° to 40°.

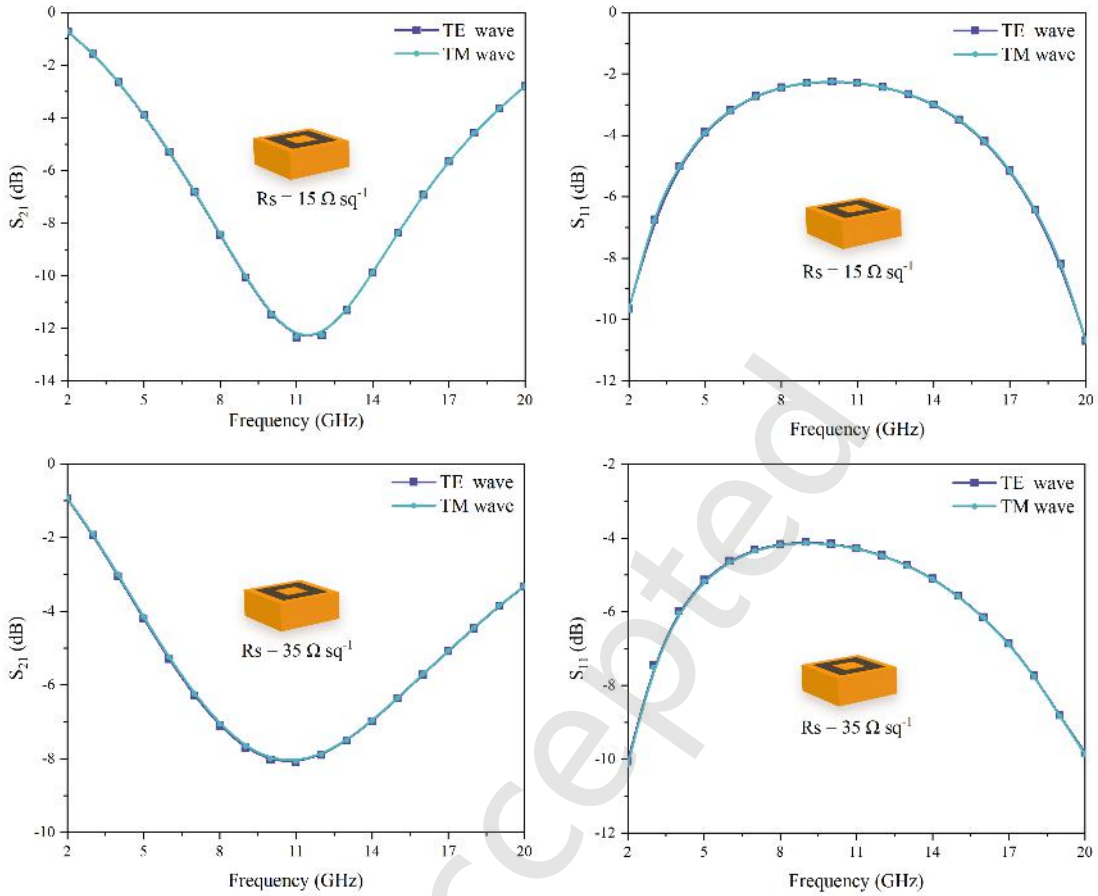

Figure S7. Simulated S_{21} and S_{11} of the FSS with the sheet resistance of 15 Ω sq^{-1} (a) and 35 Ω sq^{-1} (b) under TE and TM wave.

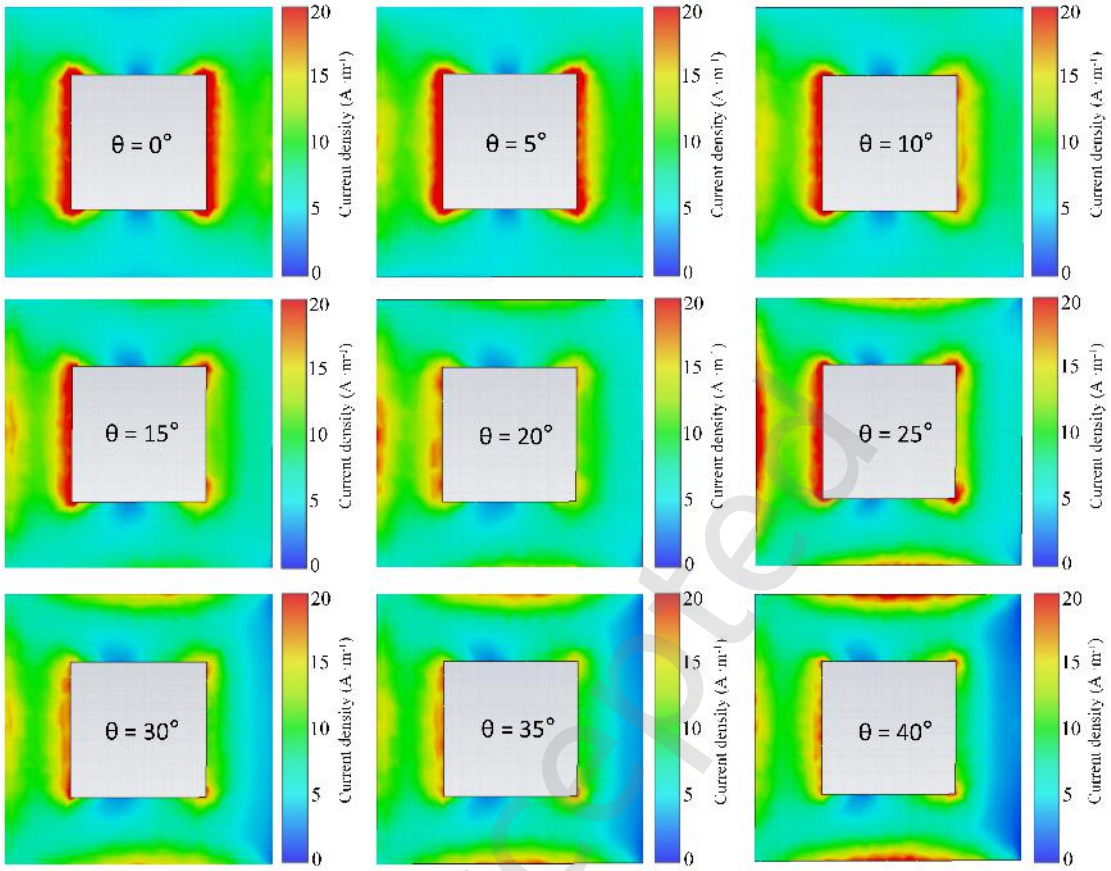

Figure S8. Current density of the FSS with the sheet resistance of 15 Ω sq^{-1} under incident electromagnetic wave angle of 0−40°.

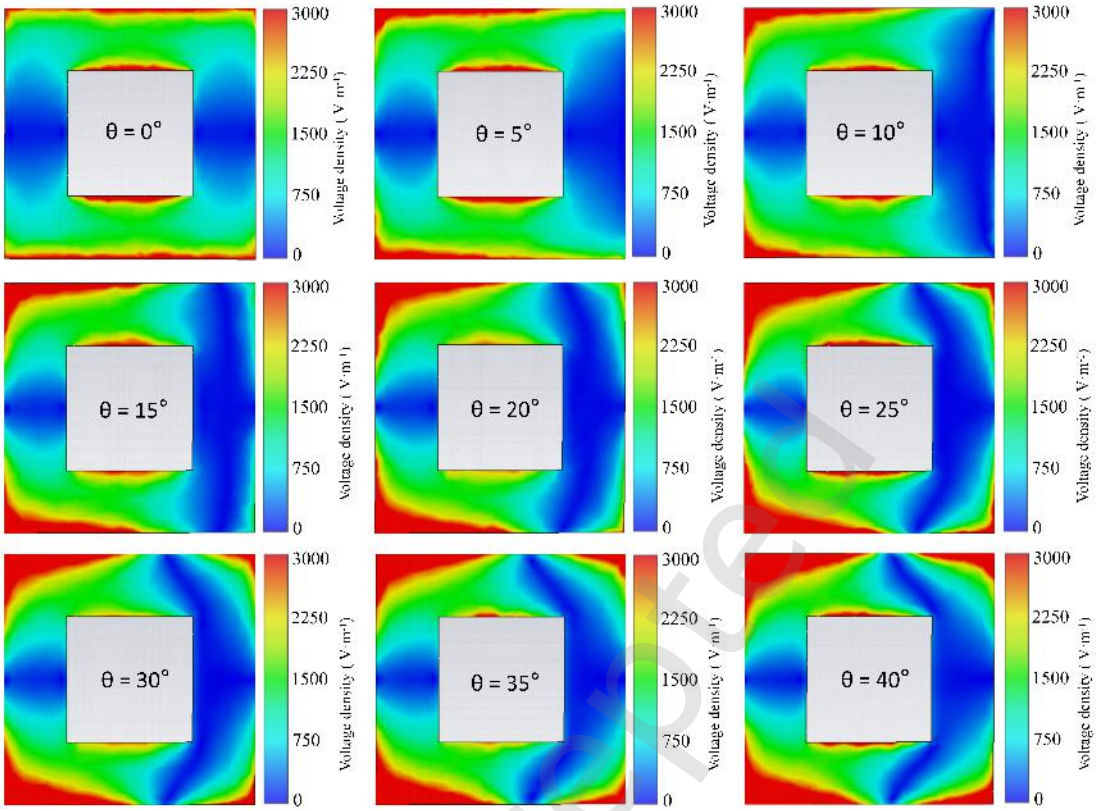

Figure S9. Voltage density of the FSS with the sheet resistance of 15 Ω sq^{-1} under incident electromagnetic wave angle of 0−40°.

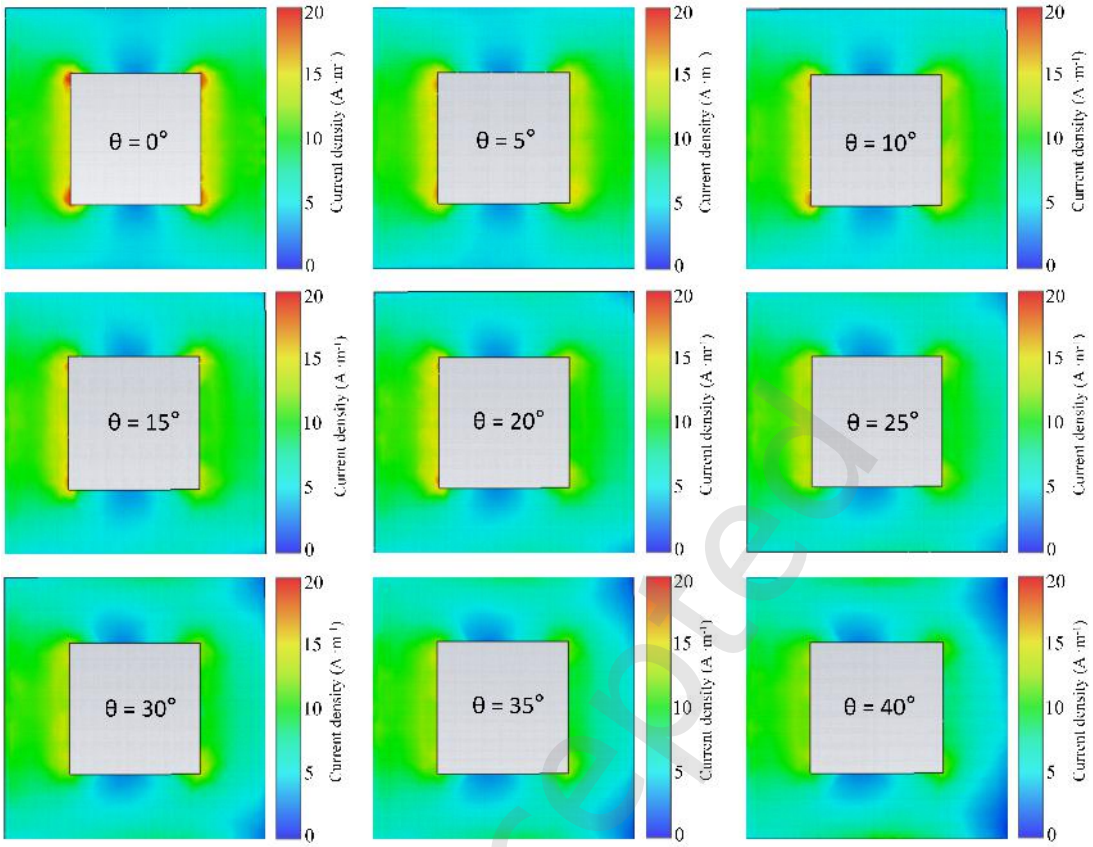

Figure S10. Current density of the FSS with the sheet resistance of 35 Ω sq^{-1} under incident electromagnetic wave angle of 0−40°.

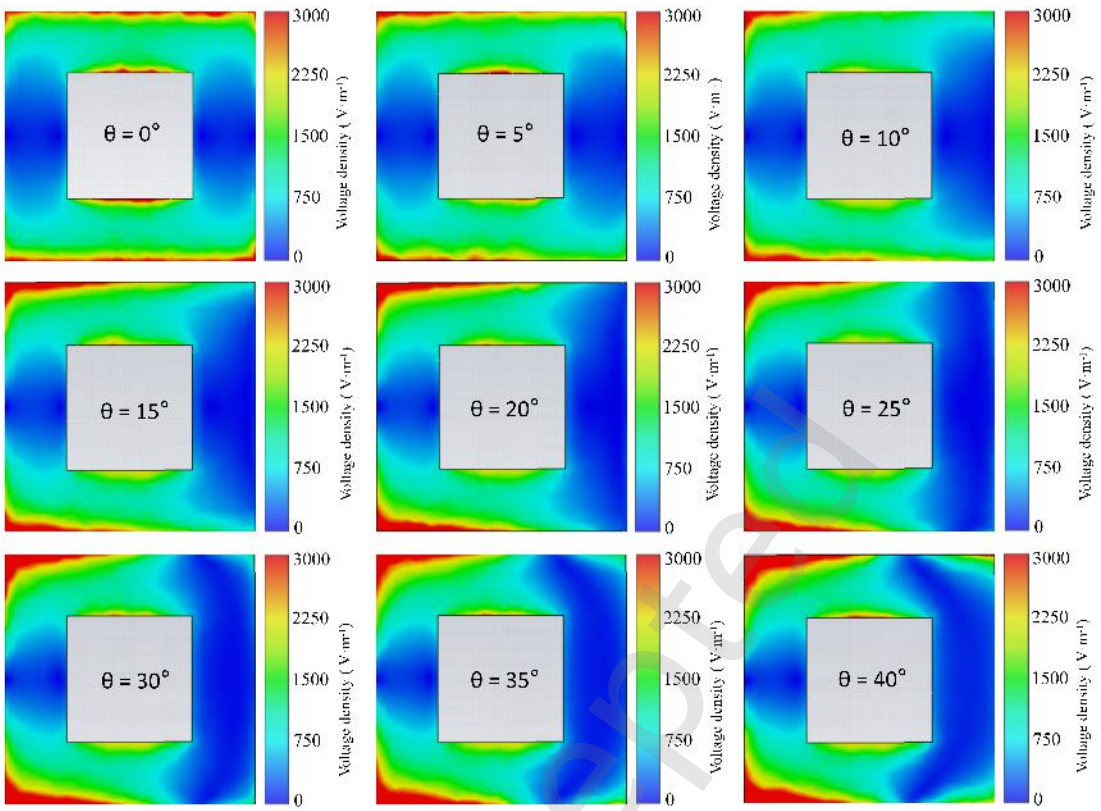

Figure S11. Voltage density of the FSS with the sheet resistance of 35 Ω sq^{-1} under incident electromagnetic wave angle of 0−40°.

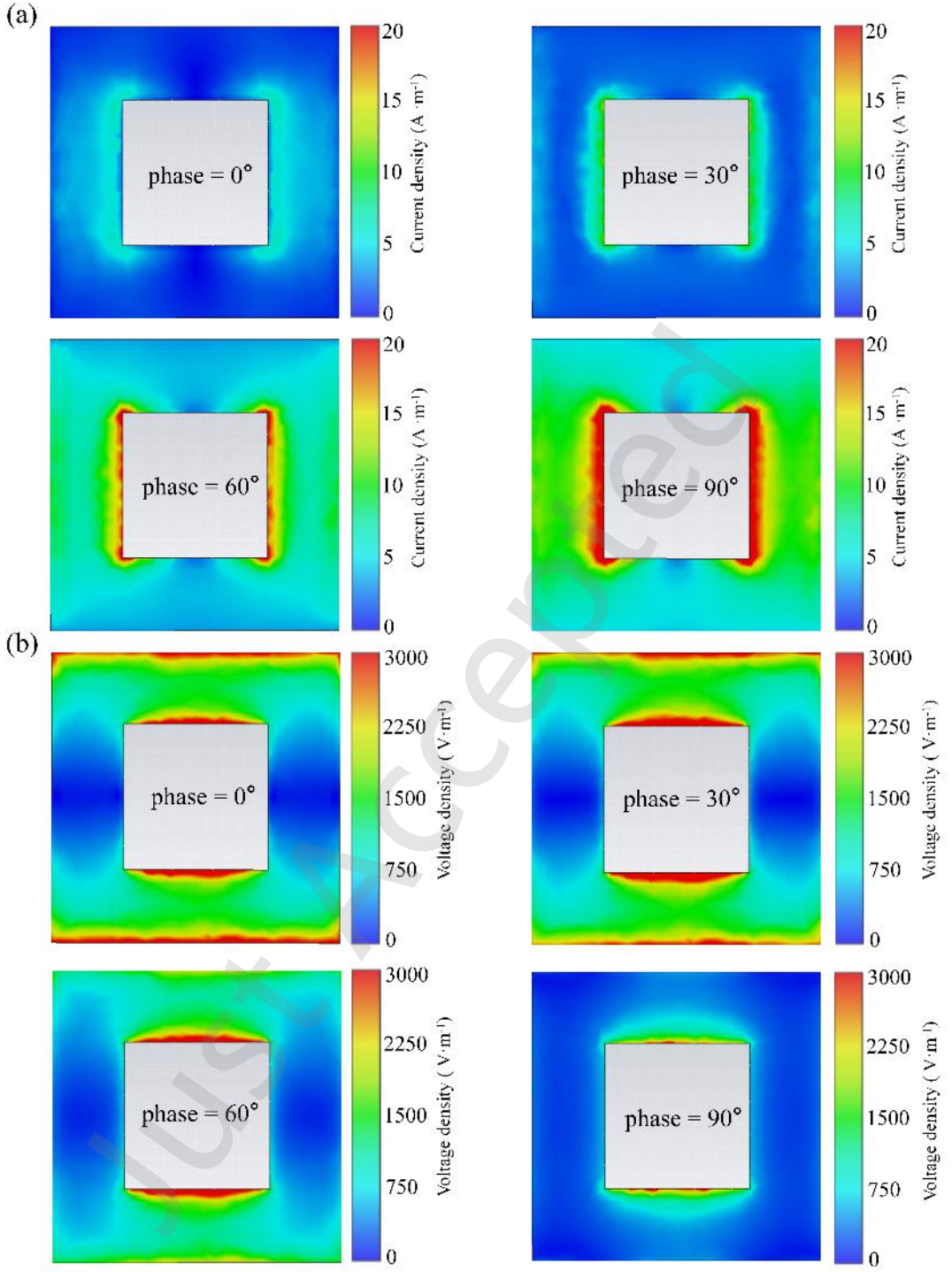

Figure S12. Current density (a) and voltage density (b) of the FSS with the sheet resistance of 35 Ω sq^{-1} in different phase.

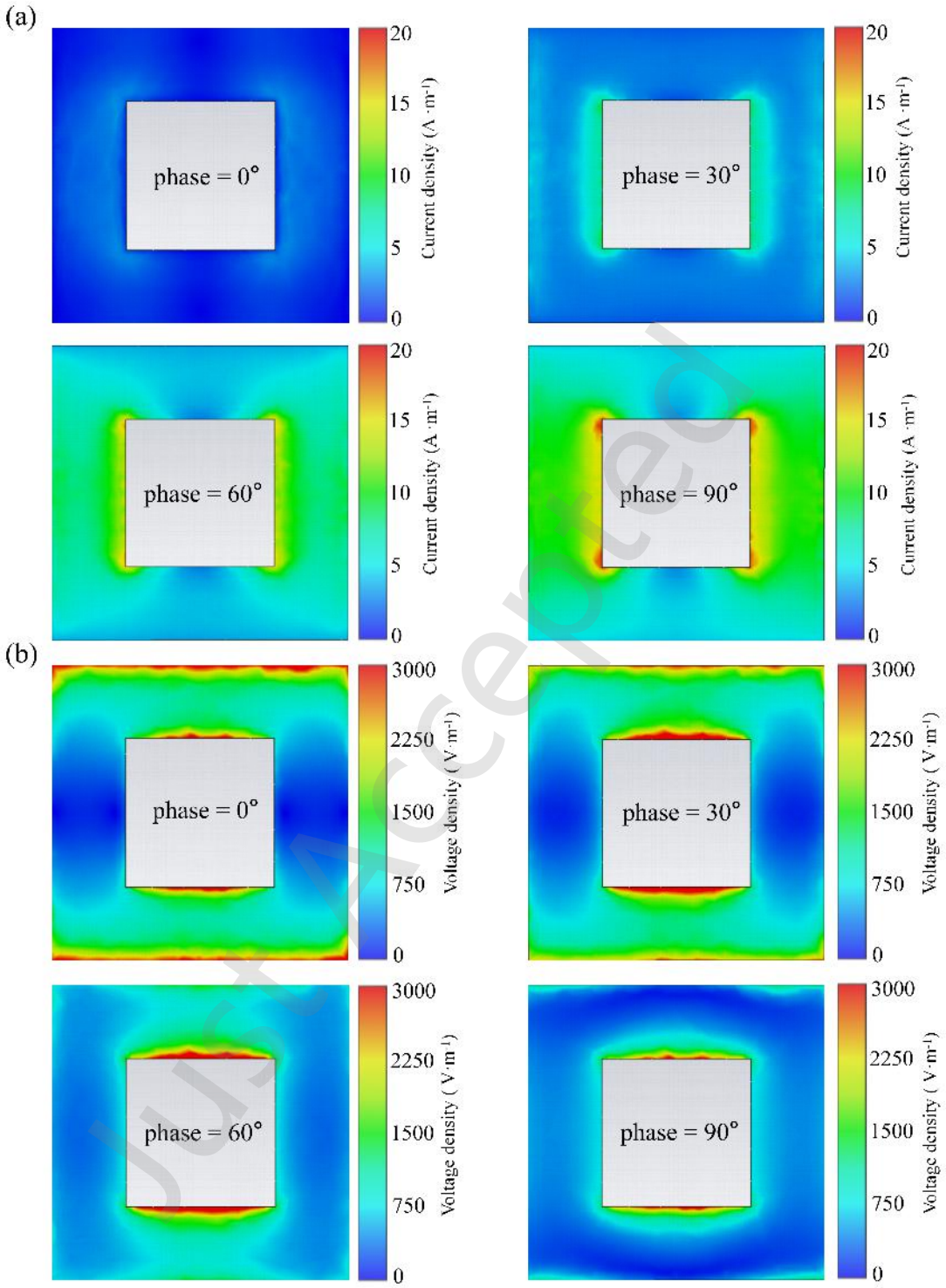

Figure S13. Current density (a) and voltage density (b) of the FSS with the sheet resistance of 35 Ω sq^{-1} in different phase.

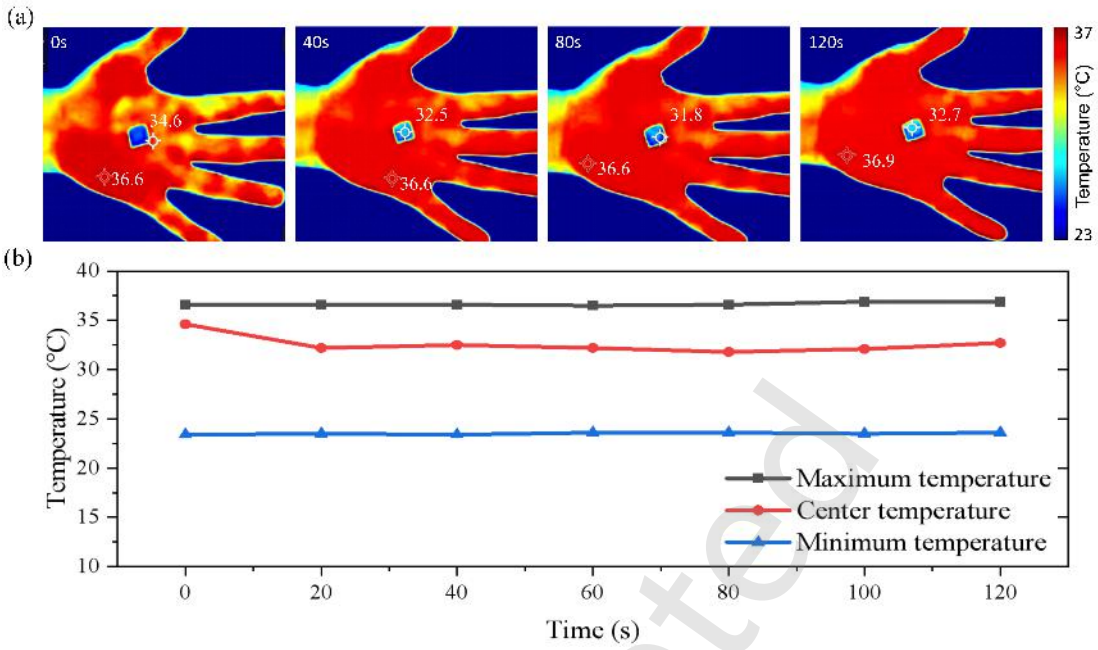

Figure S14. (a) IR images of the LSIG FSS unit placed on a volunteer's hand. (b) Variation in the maximum, minimum, and center temperatures detected at different heating times.